Interaction of the Antarctic Circumpolar Current with topography: Impacts on the Southern Ocean Eddy Dynamics

MASTERS THESIS

UNIVERSITY OF CAPE TOWN (UCT)

Nomkwezane S. Kobo

Supervisors: Prof. Chris Reason (UCT)

Dr. Pedro Monteiro (CSIR)

Dr. Steven Herbette (UCT)

April 16, 2013

Contents

List of Figures

7

List of Tables

Abstract

This work considers the influence of topography on the dynamics of the Antarctic Circumpolar Current in an idealized numerical setup consisting of a stratified ($L_d \simeq 60$ km) east-west periodic channel forced by a westward wind stress and surface heat fluxes. Using the regional modeling system (ROMS), four numerical experiments are carried out. Our sensitivity study considers a meridional ridge, a plateau, randomly scattered seamounts, and a flat bottom. We focus on the description of the mean flow and look for regions of high eddy kinetic energy (EKE). A non-dimensional analysis of the potential vorticity (PV) equation shows that the dynamics of the mean flow is governed by four non dimensional parameters: a Rossby number, a Burger number and two β numbers related to the presence of a background environmental PV gradient associated to the earth sphericity and the topography. The following work only considers large scale topography, for which the Rossby and the Burger number are small. Therefore, the mean eastward zonal flow is deviated equatorward when it impinges on the large-scale meridional ridge and plateau, following the f/h contours. In the case of scattered seamounts, the mean flow looks more like a muddle of multiple jets flowing around some more quiescent regions collocated with the position of the seamounts. As observed in nature, our numerical experiments with topography show enhanced EKE at depth. In the ridge and plateau experiments, these regions are located downstream of the obstacle and coincide with the presence of large scale stationary meanders. With a 16 km horizontal resolution and 35 vertical levels, our simulations do not show any correspondence between regions of high EKE and regions of higher vertical mixing. Nevertheless, this work is a first step towards a more extensive study aiming at understanding how the presence of topography may trigger upward vertical fluxes in the Southern Ocean, which in turn could uplift iron towards the euphotic zone, enhance primary production, and hence play a role in the uptake of atmospheric CO_2 by the Ocean.

PLAGIARISM DECLARATION

I know the meaning of plagiarism and declare that all of the work in the dissertation (or thesis), save for that which is properly acknowledged, is my own. Aside from guidance from my supervisors, I have received no assistance, except as acknowledged.

Supervisors:

Professor Chris Reason: Department of Oceanography, University of Cape Town (UCT), South Africa.

Dr Steven Herbette: Department of Oceanography, University of Cape Town (UCT), South Africa.

Dr Pedro Monteiro: Council for Scientific and Industrial Research (CSIR), South Africa.

SIGNATURE:

Dedication

I dedicate this thesis to the following important people:

To **Dr Onno Ubbink**, Head of Digital Science and Technology Group, (CSIR). Thank you very much for believing in me. To me you are like an angel sent by God to look after me. No words can explain how thankful am i for all you have done in my life. Indeed to have a father it does not mean he has to be your biological one.

To **His Grace the Right Rev. Dr B.E. Lekganyane**, spiritual leader of Zion Christian Church (Z.C.C). Your pilgrims and teaching gave me strength, motivation and inspiration to keep on studying further. Ke ya leboga "Kgomo". This document is one of the outcomes of your words.

To my family (**Pinkie Betty Kobo** (mother), the late **Fanyane Johannes Kobo** (father), my siblings (Ngwato, Refilwe, Kleinbouy, Makeko, Sheilla, Portia and Sinah), my nephew Bongani and nieces (Queen, Katlego and Moagi)). Thank you for your love and moral support throughout my studies.

Acknowledgements

I would like to pass my sincere gratitude to the following people and organizations for their contribution towards the completion of my thesis:

My supervisors: Dr. Steven Herbette, Dr. Pedro Monteiro and Prof. Chris Reason. Thank you all for driving me throughout this journey of academics as well as your fatherly advices.

I am greatful for the comments raised by external examiners.

The Southern Ocean Carbon Climate Observatory Group (SOCCO), for their positive criticism and comments. SOCCO also served as home to me (home is a place where one finds joy and peace).

Dr. Nicolette Chang, thank you for introducing me to the ROMS model and always been there for me whenever I needed your assistance, your compromise of working extra hour with me meant a lot, Nicky.

Council for Scientific and Industrial Research (CSIR) for their financial support.

Applied Center for Climate and Earth System Science (ACCESS) for their financial support.

Center for High Performance Computing (CHPC) for allowing me to utilize their facilities (clusters) to run my experiments.

Jerome, Charine, Yonns, Isufu and everyone at the Oceanography Department, UCT.

Introduction

The Antarctic Circumpolar Current (ACC) is the dominant circulation feature of the Southern Ocean. It is a deep reaching current that transports about 134 Sv of seawater around Antarctica, between 40°S and 65°S over 24,000 km (Hughes, 2005; Cunningham et al., 2003; Sloyan and Rintoul, 2001). This makes it one of the largest ocean currents. The open geometry of the Southern Ocean makes the dynamics of the ACC markedly different from those of other ocean currents. The absence of continental barriers in the latitude band of the Drake Passage, a relatively narrow body of water between Cape Horn and the Antarctic Peninsula creates a periodic zonal pathway that allows the current to flow zonally around the globe. This specificity makes the ACC the unique circumpolar current found among the different Oceans. As a result, the ACC connects the three major world ocean basins (Atlantic, Pacific and Indian) and has a strong impact on the transport and distribution of tracers in the World Ocean.

Looking closer at the ACC, one realises that the ACC is not just one large and homogeneous body of water flowing eastward around the globe at high latitudes. It is associated with several fronts that can be identified by strong eastward jets and sharp horizontal gradients in water properties (temperature and salinity). These fronts are the boundaries between zones of weaker eastward flow, generally associated with uniform water properties. These features define some latitude bands that are presented in (Figure 1). From north to south, we find the Sub-antarctic Zone (SAZ), the Sub-antarctic Front (SAF), the Polar Frontal Zone (PFZ), the Polar Front (PF), the Antarctic Zone (AZ), the Southern ACC front (SF) and the Southern ACC zone (Orsi et al., 1995).

The large eastward flow of the ACC is driven both by strong westerly winds over the Southern Ocean and surface buoyancy forcing (heating of the ocean at low latitudes and cooling at high latitudes). There are several water

masses found within the ACC. The Antarctic Bottom Water (AABW), originating through deep water formation in the Weddell, Ross Sea and Prydz bay flows northward at depth out of the Southern Ocean region after first being influenced by the bathymetry of the Antarctica shelf. It consists of a higher salinity branch and a lower salinity branch. It then mainly forms the deepest layers of the Southern Ocean. The North Atlantic Deep Water (NADW) and Circumpolar Deep Water (CDW) flow in the Southern region in between 2000 m and 4000 m depths. The Antarctic Intermediate Water (AAIW) and the Subantarctic Mode Water (SAMW) both flow equatorward, the latter in the upper thermocline.

The dynamic signature of the ACC extends over the whole water column, as a result bathymetry will have strong impact on the path of the ACC itself. The influence of bottom topography on oceanic flow is such that it can change the path of large scale currents such as the ACC and play an essential role in the vertical distribution of momentum (Gille, 1997). Topography can also impact the flow pattern at the synoptic scale. It can cause the generation of eddies, deflection of the flow field (McCartney, 1976) and create sacs of trapped fluid such as Taylor columns (Lavelle and Mohn, 2010). Topographic features can also affect the energy balance of large scale currents by exerting drag on the flow (Hughes, 2005). Other features which are exhibited at shorter time and space scales than synoptic, are topographic rectification of tidal motions, internal wave trains, enhanced boundary mixing, and the generation of trapped topographic waves (Hovius et al., 2011). Therefore it is important to understand the effect of topographic features, because they can influence ocean circulation over a wide range of time and space scales (Thompson and Salée, 2012).

This study aims at investigating the generation and fate of eddies by the interaction of the ACC with topography. The study analyses the potential vorticity of the ACC and the EKE of the Southern Ocean. Three topographic features were considered, a ridge, a plateau and scattered seamounts. All may affect the eddy dynamics of the Antarctic Circumpolar Current and consequently the surface mixed layer of the Ocean.

This study used an idealised configuration of the ACC using the Regional Ocean Model System (ROMS) to simulate the interactions of the ACC with

topographic features in an east-west periodic channel (cyclic boundary conditions). The idealised model simulations were forced by stationary (constant in time) westerly wind and surface heat fluxes, both varying in latitude in order to mimic the spatial distribution of the annual climatology in the Southern Ocean. Four scenarios were considered in order to test the different topographic features on the ACC:

- 1st: The ACC flowing in a flat bottom.

- 2nd: Flow of the ACC across a meridional ridge.

- 3rd: Flow of the ACC across a plateau.

- 4th: Flow of the ACC across randomly scattered seamounts.

We diagnose:

- Rossby number (Ro) and Burger number (Bu) to describe the characteristics of the flow patterns and strength of stratification respectively.

- the eddy kinetic energy (kinetic energy resulting from perturbations).

A comprehensive literature review is presented in the next chapter. In this chapter backgroud study of the Southern Ocean is reviewed. This is followed by the methodology of numerical modelling approach and experimental set-up, which are discussed separately and in detail. In Chapter 3, the results of the numerical modelling are presented and analyzed collectively. In chapter 4, the development of the theory used to interpret our results is established and results are interpreted using the theory. Chapter 3 and chapter 4 are later incorporated together into the Discussion and Conclusion chapter. Finally, recommendations are also included in Chapter 5. Then, the appendix.
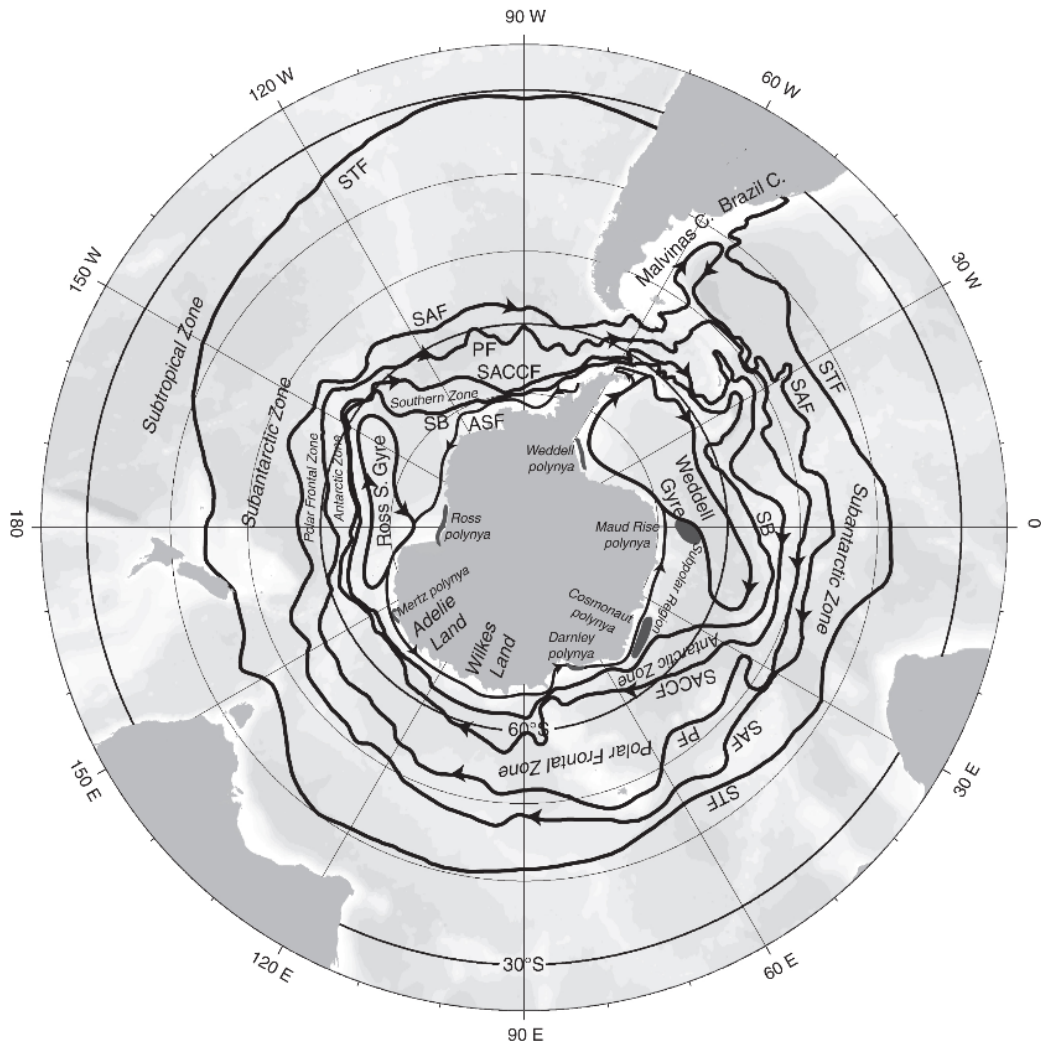
Figure 1: Illustration of fronts and zones along the ACC path in the Southern Ocean:
From **http://booksite.academicpress.com/DPO/chapter13.html**

Chapter 1

Literature review

1.1 Ocean and Climate

The ocean is the largest carbon reservoir in the global carbon cycle. It has taken up about 40% of the anthropogenic CO_2 emissions in the past two hundred years. Therefore, it is essential to better determine the carbon drivers in the ocean and how they might respond to a changing climate, in order to improve estimates of future atmospheric CO_2 levels. Air-sea gas exchange plays an important role in climate regulation by controlling the rate of CO_2 and heat uptake by the ocean. Thus, many experiments have been designed to determine the relationship between environmental variables and the rate of air-sea gas exchange. Surface boundary dynamics are critical to ocean atmosphere exchange of heat and CO_2. Globally, the dominant control of air-sea gas exchange is turbulent energy delivered to the boundary interface by wind. The latter may vary with climate change.

Analysis of global warming over the past few years all show warming of the ocean (Levitus et al., 2005). More than 85% of the total increase in heat stored by the Earth system has gone into warming the ocean with much smaller amounts of energy going into warming the atmosphere and land surface or into melting of ice (Levitus et al., 2005). A significant part of the excess heat trapped by the Earth system is being stored by the Southern Ocean.

1.2 The Southern Ocean and its role on the Earth Carbon cycle

The Southern Ocean (SO) plays a key role in the Earth's climate system (Volkov et al., 2010; Lui and Curry, 2010; Meredith et al., 2012). This region of the world ocean assimilates large amount of CO_2 released by human activities, with about 40% of the total ocean inventory of anthropogenic CO_2 found south of 30 °S (Sabine et al., 2004). It is one of the few areas of the world's ocean where surface waters are dense enough to sink into deep ocean. These waters take up CO_2 from the atmosphere, and by sinking into the deep ocean they effectively pump it into the deep ocean. The region is also known to be an important sink for atmospheric heat and CO_2. The rate of atmospheric CO_2 export into the deep Southern Ocean is controlled by two mechanisms:

- the solubility pump,

- the biological pump,

1.2.1 Solubility pump

The solubility pump is the process through which the ocean removes atmospheric CO_2 as air mixes with and dissolves into the upper ocean. Since carbon dioxide is more soluble in cold water than in warm waters, cold surface waters found at high latitudes are able to absorb more carbon than the warm surface waters found at low latitudes. The global Ocean circulation plays an important role in controlling the time for which the atmospheric CO_2 absorbed by the ocean at high latitudes can remain stored within the ocean before being released into the atmosphere. Because the Southern Ocean is a region of deep water mass formation, one expects this atmospheric carbon to be advected into the deep ocean and remain stored for a long time. Nevertheless, vertical mixing will eventually bring the water back to the surface in regions distant from where the carbon dioxide was first absorbed. If this mixing occurs in tropical regions, characterized by warm surface waters with low CO_2 solubility, carbon rich waters will release their CO_2 back into the atmosphere.

One may consider the ocean carbon cycle on the Meridional Overturning Circulation (MOC, Figure 1.1). At high latitudes, the Ocean tends to remove CO_2 from the atmosphere and sequester it into the deep layers of the
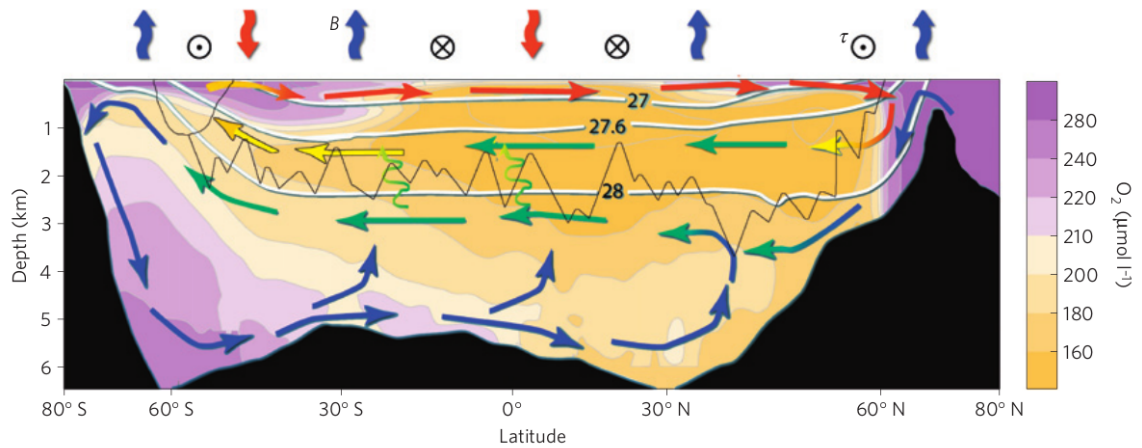
Figure 1.1: A schematic diagram of the Upper Cell and Lower Cell of the global MOC emanating from, respectively, northern and southern polar seas. The zonally averaged oxygen distribution is superimposed, yellows indicating low values and hence older water, and purples indicating high values and hence recently ventilated water. The density surface 27.6 kg m^{-3} is the rough divide between the two cells (neutral density is plotted). The jagged thin black line indicates roughly the depth of the Mid-Atlantic Ridge and the Scotia Ridge (just downstream of Drake Passage) in the Southern Ocean. Low-latitude, wind-driven shallow cells are not indicated. General patterns of airsea surface density (equivalent buoyancy) flux, B (red or blue indicating that surface waters are being made less or more dense, respectively; broad pattern of zonal surface wind stress, τ, ⊙: eastward; ⊗, westward). Coloured arrows schematically indicate the relative density of water masses: lighter mode and thermocline waters (red), upper deep waters (yellow), deep waters including NADW (green) and bottom waters (blue). Mixing processes associated with topography are indicated by the vertical squiggly arrows. Adapted from **Marshall and Speer (2012)**

.

Ocean through the down-welling branches. On the other hand, the upwelling branches will contribute to the release of CO_2 to the atmosphere (Le Quérée et al., 2007; Rintoul et al., 2012). Hence, the balance between the upwelling and downwelling branches of the Southern Ocean overturning circulation serves as one of the important components in determining how much carbon dioxide is absorbed and stored by the ocean. Other sources contributing to high inventory of anthropogenic CO_2 in this region are cooling and sinking of subtropical waters (Rintoul et al., 2012).

1.2.2 Biological pump

The biological pump (Figure 1.2) refers to the processes by which phytoplankton consumes dissolved inorganic nutrients and CO_2 during photosynthesis

and collectively absorbs these elements into organic material. The latter is then exported largely by gravitational settling into the deep sea (Anderson et al., 2002). About half of the biological production on Earth occurs through photosynthesis of phytoplankton.
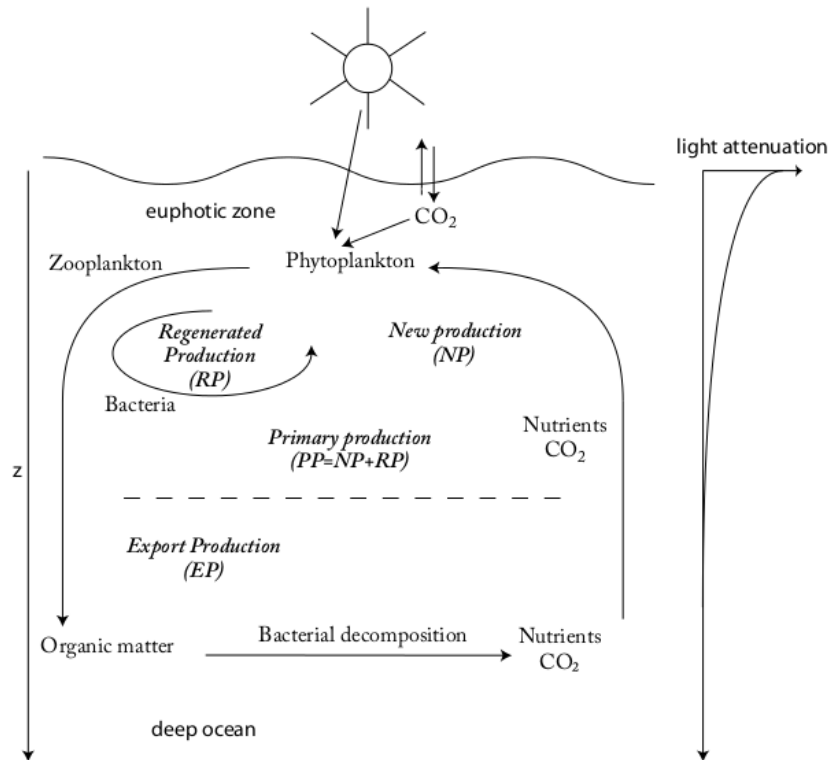
Figure 1.2: A Schematic representation of the biological pump in the ocean. Adapted from **Lévy (2008)**

Primary production is at the base of the ocean food chain (Shaffer, 1993). Almost all marine life relies on this primary production. It also plays an important role in the global carbon cycle because phytoplankton growth, and the subsequent death and sinking of organic matter, transports large quantities of carbon (3 Pgcy^{-1}) out of the surface layer, in the deep Southern Ocean where it can be sequestered for long times (Lévy, 2008; Shaffer, 1993).

Previous studies (Sarmiento and Toggweiler, 1984; Siegenthaler and Wenk, 1984) showed that a change in the efficiency of the Southern Ocean's biological pump could be an important potential source of variability for the atmospheric CO_2. The "efficiency" of the biological pump can be explained by the fraction of nutrients upwelled to surface waters, consumed by phytoplankton at surface, and exported as organic matter to the deep sea (Lévy,

2008). Biological unconsumed nutrients are carried back into the deep sea as preformed nutrients during the formation of deep and intermediate water masses. Consequently, the biological pump's efficiency is influenced by the rate of nutrient supply by upwelling as well as the rate of nutrient loss by biological consumption. (Anderson et al., 2002).
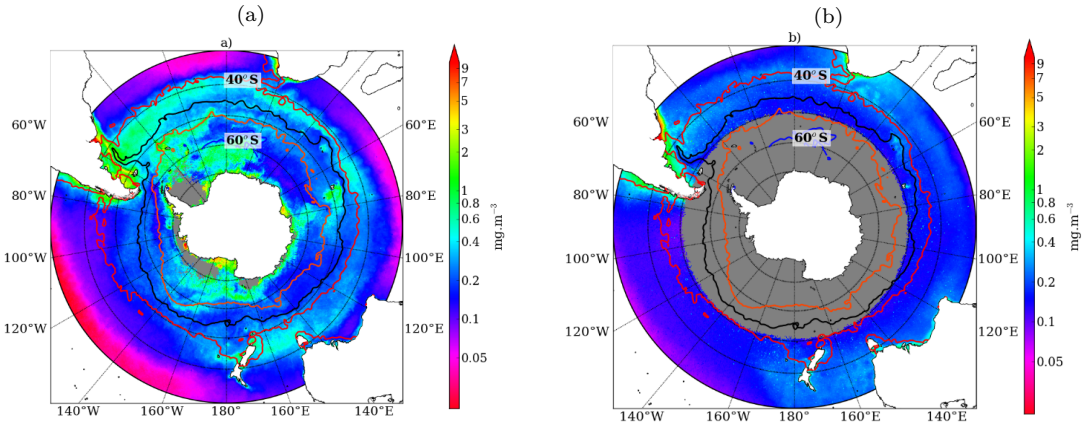
Figure 1.3: Spatial distribution of mean chlorophyll concentrations for the Southern Ocean south of 30° S for (a) summer January and (b) winter July. Lines represent the mean positions of the main density fronts of the Southern Ocean. STF (red), the SAF (black), the PF (orange) and the SACCF (blue). Adapted from **Thomalla et al. (2011)**

The Southern Ocean biological pump also plays an important component in regulating the supply of nutrients to the thermocline waters (Subantarctic Mode Water and Intermediate Water) of the whole Southern Hemisphere and of the North Atlantic Waters. In turn, this supply drives the low latitude productivity (Thomalla et al., 2011). The Southern Ocean is characterized by the largest residual stock of unused macronutrients, but low average phytoplankton standing stocks, with diverse temporal and spatial variability in the phytoplankton biomass (Fauchereau et al., 2011; Thomalla et al., 2011; Tagliabue et al., 2012).

Satellite data shows that there is strong spatial and inter-annual variability in the primary production of the Southern Ocean. The regions of the Southern Ocean respond differently to that variability (Figure 1.3). Thomalla et al. (2011) studied this inter-annual variability using the mode referred to as the seasonal cycle. Seasonal cycle is the mode through which, the physical mechanisms of climate forcing are coupled to ecosystem responses such as productivity, diversity and carbon export (Lévy, 2008). Thomalla et al. (2011) showed that this mode does not fully explain the inter-annual variability of the Southern Ocean primary production.

21
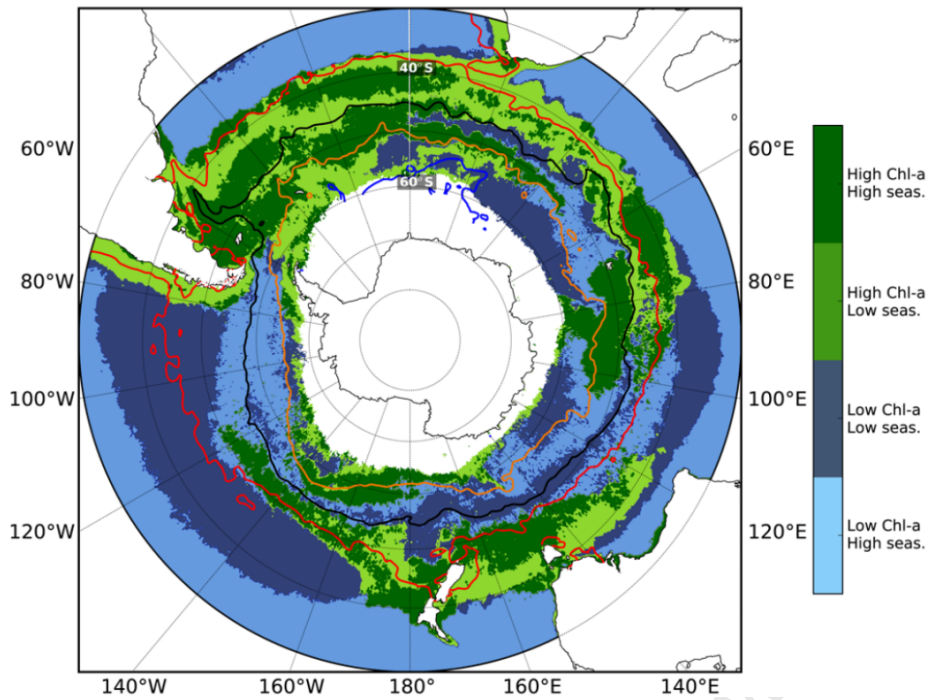
Figure 1.4: A schematic diagram summarizing the response of phytoplankton biomass to the underlying physics of the different seasonal regimes. This figure shows that different regions of the Southern Ocean respond differently to the seasonal cycle. Regions highlighted in green show strong correlation between high primary production and regions of enhanced EKE (e.g. region like the Kerguellen plateau). Colorbar explains the behavior of each region in response to the seasonal cycle. Regions in green represent regions of high chlorophyll concentration with either high seasonal cycle reproducibility (dark green) or low seasonal cycle reproducibility (light green). Adapted from **Thomalla et al. (2011)**

Several mechanisms related to sea ice or mean flow-topography interactions may explain the spatial heterogeneity and patchiness that is observed in the chlorophyll distributions. For example, sea ice may influence the efficiency of the primary production through direct effects, such as the attenuation of incident solar radiation, or indirect effects such as the perturbations of air-sea gas exchange, and locally induced dynamical and thermodynamical processes (Lévy, 2008). Thomalla et al. (2011) observed that flow-topography interactions may also influence the efficiency of the primary production. Some regions show strong correlation between the primary production and regions of enhanced eddy kinetic energy (EKE), region like the Kerguellen (50-55° S, 70-75° E; Figure 1.4).

1.2.3 Summary

In the Southern Ocean, the role played by physical forcing in enhancing chlorophyll is still not well understood and requires further investigations. It is important to first understand local dynamics, such as mechanisms generating EKE, in order to better understand the response of the ocean carbon cycle to changing climate.

1.3 The Southern Ocean Circulation

1.3.1 Mean flow

The ACC transports approximately 134 Sv (1 Sv = 10^6 m^3 s^{-1}) around the world between approximately 40°S and 65°S (Cunningham et al., 2003). The maximum flow of the current is normally concentrated between two roughly parallel fronts, the Subantarctic Front and the Polar Front, with the Polar Front being closer to the Antarctic continent (Figure 1.6). There are two prevailing viewpoints about what determines the ACC transport: Stommel (1957), suggested that the ACC transport is controlled by Sverdrup balance Sverdrup (1947) . The wind stress curl to the north of Drake Passage drives a poleward transport, which Stommel argued passes through Drake Passage and returns equatorward in a western boundary current, the Malvinas Current. In contrast, Straub et al. (1993), and others have suggested that the ACC transport is controlled by the angular momentum budget, which involves a complex interplay between surface wind forcing, buoyancy forcing, eddy fluxes, and friction (Peterson and Whitworth, 1989). Gnanadesikan and Hallberg (2000) and Gent et al. (2001) showed that water mass transformation can alter the ACC transport and thus they concluded that ACC transport is neither determined by Sverdrup balance nor the mean wind stress.

Hence, attention has centered on the angular momentum (or zonal momentum) balance rather than on Sverdrup balance. However both have been considered. Munk and Palmén (1951) showed that pressure forces on the ocean bottom topography are the most likely candidates to balance the angular momentum input by zonal wind stress. Gille (1997) used scaling analysis to show that other possibilities like bottom or lateral friction, or the nonlinear advection of angular momentum are very small. In this zonal and depth

integral balance, the Coriolis force drops out if there is no steady north-ward mass flux across each latitude, and becomes small for realistic mass fluxes due to evaporation and precipitation (Peterson and Whitworth, 1989). The remaining term is the pressure force on topographic obstacles. Earlier studies estimated that the zonal wind stress could be balanced by bottom pressure in the Southern Ocean if the pressure was higher on the western side of ridges than on the eastern side by an equivalent 4 cm of water for a series of ridges with height adding up to 10 km (Munk and Palmén, 1951). It has recently been accepted that, in the Southern Ocean, zonal wind stress is mainly balanced by bottom form stress (Hughes and De Cuevas, 2001). Munk and Palmén (1951) pointed out that this might provide a link between wind stress and the transport of the Antarctic Circumpolar Current (ACC), implicitly assuming that the form stress could be interpreted as a form drag associated to the strength of the zonal flow at the ocean floor. Even though the Coriolis force drops out in the depth and zonal integral, this is not the case for the zonal integral at each depth. Angular momentum input into a near-surface layer by zonal wind stress generates a northward flow, allow-ing Coriolis to balance the wind stress. Consequently, mass conservation requires a return flow at depth in which an equal and opposite Coriolis force must be balanced by a pressure force (form stress). This clearly shows that the balance between wind stress and form stress is closely connected to the meridional overturning circulation. However, it is not clear if it is related to the strength of the ACC (Hughes and De Cuevas, 2001).

Even though attention in the Southern Ocean is given to the balance between wind stress and bottom form stress, it has to be applicable at all latitudes. At latitudes outside the Drake Passage, there can be no mass trans-port across each latitude circle, making the Coriolis force negligible in the integral over longitude and depth (Hughes and De Cuevas, 2001). The zonal wind stress is then balanced by the pressure difference across topographic features. This balance can be interpreted as a meridional overturning cell with northward flow in the Ekman layer and a geostrophic return flow at depth, or the other way round. Hughes and De Cuevas (2001) also, indicate that a change of pressure along an isobath leads to a bottom pressure torque, which must upset the Sverdrup balance (Hughes and De Cuevas, 2001). This implies an important role played by topography in gyre circulations and a

relationship between form stress and Sverdrup balance that applies in the Southern Ocean.

Major topographic features across the ACC path
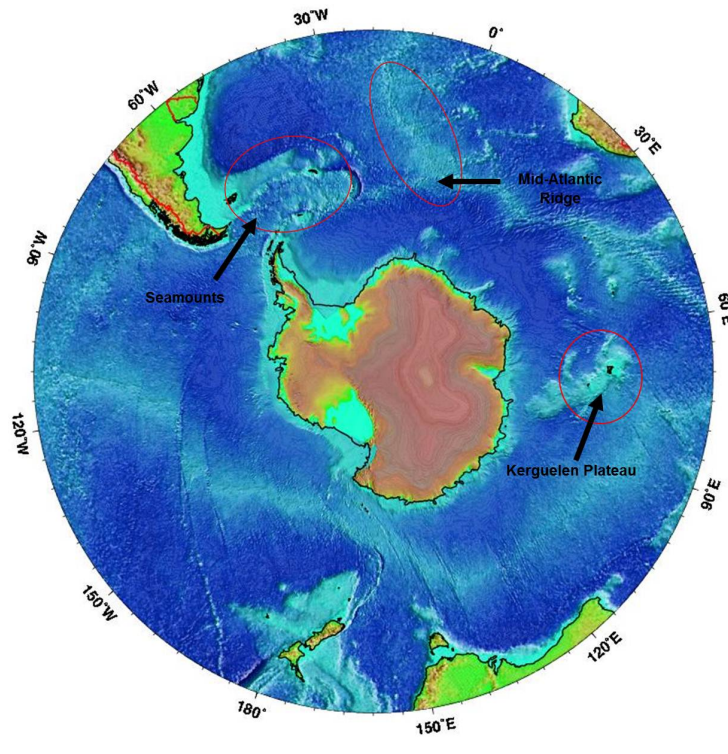
Figure 1.5: Southern Ocean bathymetry. From **google-images**

-

Figure 1.5 shows a map of bathymetry in the Southern Ocean. At the latitude band of the Drake passage, many topographic obstacles may alter the paths and the dynamics of the ACC. The Atlantic sector holds the most variable topography. Many scattered seamounts and islands can be found all along the AAC path, the most prominent ones being located just west of the Drake passage.

The most prominent topographic feature found in the Southern Indian Ocean is the Kerguelen plateau, that literally obstructs the zonal path of the ACC. The Atlantic-Indian Basin forms part of the Atlantic and Indian Ocean sectors and is connected with the Weddell Sea to the west and the Kerguelen Plateau to the east.

25

Generally, the generation of eddies occurs where topographic features are located (McCartney, 1976). Downstream of the Scotia Ridge, the eastward flow is increased and then becomes highly turbulent. Part of this water follows the continental shelf of South America, forming a Malvinas Current, a western boundary current that collides with the south Brazil Current forming the Confluence Zone which, is one of the most energetic areas in the world. This region is close to the Argentine Basin, which is characterized by a depth of more than 6000m and is bounded by a very steep continental slope. In the middle of the basin, a sedimentary deposit is located, the so-called Zapiola Rise (ZR), whose top is about 1000 m higher than the abyssal plain. This particular topography creates a very intense counterclockwise barotropic flow, i.e. the Zapiola Anticyclone (Saunders and King, 1995) which is likely to be an important mechanism in the exchange of heat between the Southern Ocean and lower latitudes (de Miranda and Dewar, 1999).

1.3.2 Dynamics of the ACC

In order to reproduce a consistent ACC in a model, it is useful to first gain some knowledge on its dynamics and be aware of some puzzling questions that have been debated among the scientific community. It is well known that the ACC is forced by strong westerlies and buoyancy heat forcing (Abernathey et al., 2011).

- In the absence of boundaries, one may wonder what prevents this zonal flow from accelerating indefinitely, being continuously fed with momentum by the westerly wind stress along an unclosed band of latitude.

- Another puzzling question concerns, what balances the northward Ekman flux generated by these continuous westerly winds blowing along the ACC?

- Finally, one may be interested in knowing why the ACC is a deep reaching current while most other ocean currents have a weak signature at depth.

The dynamics of the ACC are complex and strongly depend upon interactions between mesoscale (synoptic) eddies, topography, and the mean flow (Wolff et al., 1991). Munk and Palmen (1951) were the first to describe the recently general accepted view that topographic form stress balances the
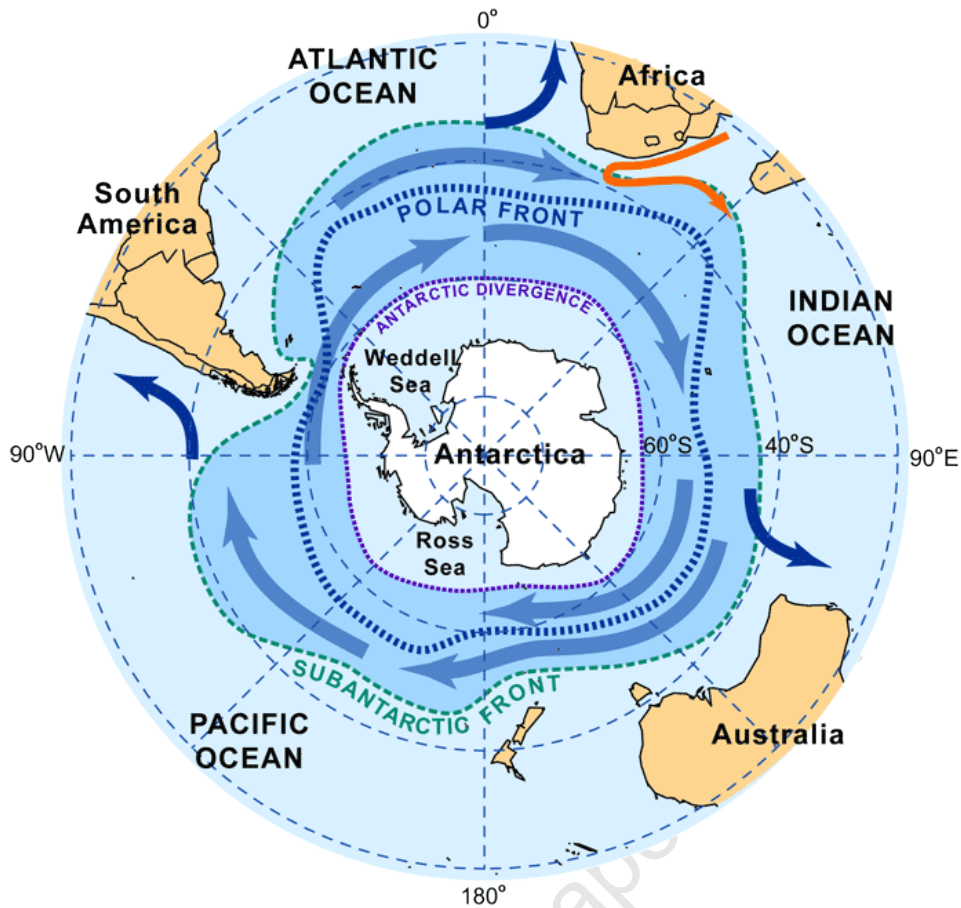
Figure 1.6: Schematic of the Antarctic Polar Front which, marks the location where Antarctic surface waters moving northward sinks below warmer sub-antarctic waters. And, further north (away from Antarctica) is the Sub-antarctic Front, the boundary between the Southern Ocean and the warmer Atlantic, Pacific and Indian oceans. The main flow of the Antarctic Circumpolar Current occurs between these two fronts (darker blue area). From **http://www.noc.soton.ac.uk/o4s/euroargo/atour/a410drake**

wind stress. Gille (1997) confirmed this view by investigating the momentum balance of the ACC using both output from a high resolution primitive equation model and sea surface height measurements from the Geosat altimeter and found that topographic form stress is the dominant process balancing the surface wind forcing. Detailed examination of form stress in their model indicated that it is due to three large topographic obstructions: the Kerguelen Island, the Campbell Plateau, and the Drake Passage. The flow could establish a pressure on the western side of the topographic features. The difference between wind stress and form stress represents the lateral transfer of momentum into and out of the ACC (Hughes, 2005; Gille, 1997). Several studies have shown that zonal flow is strongly affected by topographic form stress (Thompson and Salée, 2012; Gille, 2003). Another component of the

27

flow is the presence of mesoscale eddies that transfer the surface stress to the bottom where it is dissipated by the topographic form stress(Hughes, 2005).

1.3.3 Eddies in the Southern Ocean

Recent studies of the Southern Ocean show a region of intense mesoscale activity (Lévy, 2008). Wave number spectra of kinetic energy shows a peak around 100 km (Scott and Wang, 2005).

Southern Ocean eddies develop from barotropic and/or baroclinic instability (Treguier et al., 2007) of the ACC front itself. The northward Ekman transport induced by the wind stress acts to tilt the isopycnals towards the south. This tilting gives rise to the geostrophic component of the ACC, and allows available potential energy to be stored (Farneti et al., 2010). The stored potential energy is then released by baroclinic instability, through the spawning of eddies, whose overall effect is to flatten the isopycnes by increasing the mixing of tracers through the ACC front (Marshall and Radko, 2003; Gille, 1997).

Topography may also play a significant role in the generation of mesoscale turbulence in the Southern Ocean. Our study will focus on those effects, and we will develop this part further. Eddies are also observed to be more dominant downstream of major topographic features in the Southern Ocean (Thompson, 2010; Thompson and Salée, 2012).

Recent studies also show the presence in the Southern Ocean of remote eddies, like the Agulhas rings whose presence may contribute significantly to the eddy field observed in Southern Ocean and the southward heat transport (Swart et al., 2008).

1.4 The role of topography: Motivation

In the Southern Ocean, the seasonal cycle does not fully explain the variability of the primary production. Some regions of high EKE correspond to high chlorophyll concentrations but to low seasonality. Therefore, eddies may explain the variability of primary production in those regions. There are several mechanisms that generate EKE in the Southern Ocean. One of them is current-topography interaction. We can distinguish two main classes of processes at play. 1) When impinging on topographic obstacles, the ACC may generate a mesoscale eddy field, which in turn may trigger vertical ve-
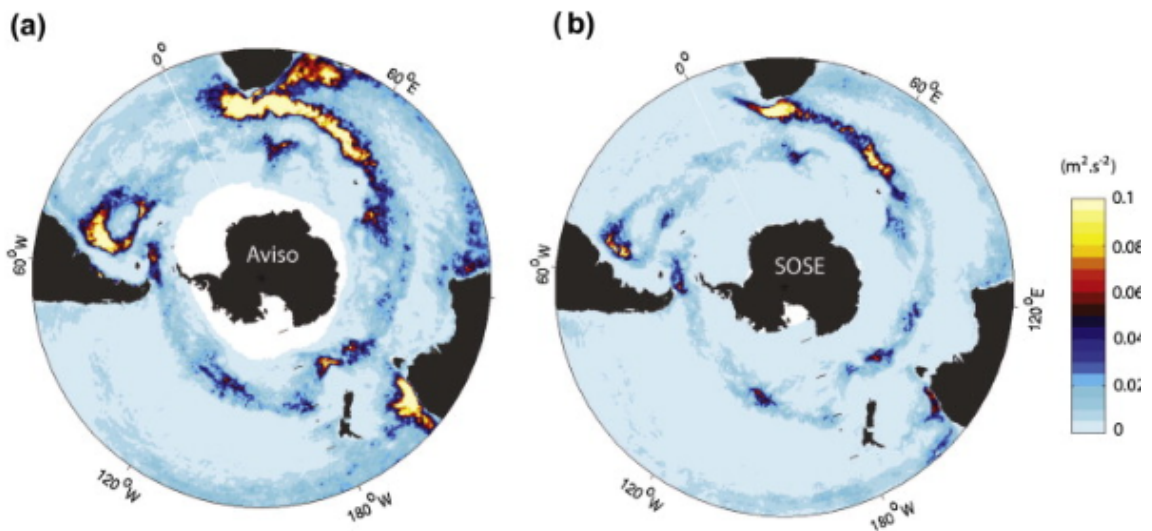
Figure 1.7: Eddy Kinetic Energy (EKE) from (a) Satellite and (b) Model. Adapted from **Rintoul and Jean Baptiste (2011)**

locities capable of uplifting nutrients to the surface. These are relatively slow processes, associated the vortical modes of the flow (*i.e* that are associated with relative vorticity). They are related to the stretching of a water column when it passes over a topographic feature. 2) When the ACC impinges on a specific bathymetry, it may also generate internal waves, capable of propagating upward to low depth. These waves may break and enhance vertical mixing, capable of uplifting iron towards the surface mixed layer, which in turn could induce primary production.

Verron and Le Provost (1985) and Herbette et al. (2003) and many others showed that when a current impinges on a seamount, two opposite sign eddies appear. An anticyclone is formed upstream or trapped above the topographic feature due to the displacement of low potential vorticity (PV) water columns from the deep ocean upon the seamount and a cyclone is formed downstream of the seamount due to the advection of high PV water columns off the topography. They also showed that between the two opposite sign eddies a strong jet like current is formed. Hughes and De Cuevas (2001) showed that the pattern of the depth-integrated flow should tell us about the vertical velocity at the ocean floor. Sallèe et al. (2008) found that in the western boundary currents extending into the Southern Ocean, mixing was approximately constant but significantly linked to EKE. Griesel et al. (2010) argued that EKE alone does not adequately describe mixing struc-

29

ture, particularly with respect to depth dependence, and they find no depth enhancement.

McWilliams et al. (1978) showed that the resolved eddies can provide interior fluxes of momentum and potential vorticity that have an important feedback on the mean flow. Wolff et al. (1991) examined the relative role of standing and transient eddies using the same model with different topographic ridges. They found that, eddy-induced mixing may be mainly localized, in western boundary currents and their extensions, gyre boundaries (Wiggins, 2005) or regions with strong interior topography (MacCready and Rhines, 2001). Lu and Speer (2010), showed that topography strongly shapes the spatial structure of flow and eddy mixing in the Southern Ocean.

The mean current speeds at which mixing is strongest are generally larger and more scattered in the cases with topography than in the cases with no topography (Lu and Speer, 2010). The mid-depth enhancement of eddy mixing seems to be associated with the interaction of topography and multiple jets embedded in the ACC. This diagnosis led Lu and Speer (2010) to suggest that topography plays a fundamental role in enhancing mixing and expanding the mid-depth eddy-mixing in the Southern Ocean, and concluded that the mechanism for this influence on the vertical structure of mixing is not clear. Preliminary analysis suggests enhanced eddy mixing over topography is, in places, due to locally enhanced baroclinicity and instability within the wake itself, at least partly due to the mean convergence of eddies in merging branches of the ACC. Interaction of barotropic and baroclinic eddies may be important in setting the greater strength and vertical structure of eddy mixing associated with topography (Witter and Chelton, 1998). Eddy mixing and diffusivity is thought to be essential in setting the strength of transport by ACC and of the overturning circulation (Thompson, 2010).

Recently, Thompson (2010) analyzed the scale and shape dependence of the role of topography in eddy transport and mixing, and found that the whole structure of mixing is itself a complex dynamical phenomenon, even over relatively smooth topography. The bending, splitting, merging, etc. of the jets, in the presence of topography may narrow the scale of time-mean jets. Lu and Speer (2010) emphasize also the discontinuous nature of the

jets, as the flow broadens or concentrates over diverse topographic slopes. Rhines (2007) suggests a slightly more generalized framework, in which the wake structure associated with topography may induce PV mixing through instability and near-zero phase speed of Rossby wave propagation.

1.4.1 Summary

To summarize, topography can alter the strength of ACC across it's path. It also plays an important role in the generation of eddy kinetic energy in the Southern Ocean, which influences the primary production of the Southern Ocean. Hence, it is important to do sensitivity tests on various topographic features and individually understand their strength in the generation of EKE.

Chapter 2

Experimental set-up and methodology

Introduction

We aim at investigating how the presence of topography in the Southern Ocean may impact the dynamics of the ACC and the characteristics of the mesoscale turbulence associated to the latter. Our work considers a modelling approach based on idealised numerical experiments of a jet impinging on several topographic obstacles. First, we present the basic configuration that we used to reproduce a zonal jet that has similar characteristics to those of the ACC. We then describe briefly the ROMS model that we used for our experiments. Finally, we give a few details on the experiments that were run. Results will be presented in the next chapter.

2.1 Model Configuration

2.1.1 Equations of motion

We considered an incompressible rotating stratified fluid in the framework of the Boussinesq and the hydrostatic assumptions on the β plane. The equations of motion are the classic primitive equations which, in Cartesian geopotential coordinates, write as follows:

$$\frac{\partial u}{\partial t} + \mathbf{u} \cdot \nabla u - fv = -\frac{\partial \phi}{\partial x} + \frac{\partial}{\partial z}\left(A_v \frac{\partial u}{\partial z}\right) + D_u \qquad (2.1)$$

$$\frac{\partial v}{\partial t} + \mathbf{u} \cdot \nabla v + fu = -\frac{\partial \phi}{\partial y} + \frac{\partial}{\partial z}\left(A_v \frac{\partial v}{\partial z}\right) + D_v \qquad (2.2)$$

$$\frac{\partial T}{\partial t} + \mathbf{u} \cdot \nabla T = F_T + D_T \qquad (2.3)$$

$$\frac{\partial S}{\partial t} + \mathbf{u} \cdot \nabla S = F_S + D_S \qquad (2.4)$$

$$\frac{\partial \phi}{\partial z} = \frac{-\rho g}{\rho_0} \qquad (2.5)$$

$$\frac{\partial u}{\partial x} + \frac{\partial v}{\partial y} + \frac{\partial w}{\partial z} = 0 \qquad (2.6)$$

$$\rho = \rho(T, S, P) \qquad (2.7)$$

$$(\mathbf{u} \cdot \nabla)\,\mathbf{u} = u\frac{\partial}{\partial x} + v\frac{\partial}{\partial y} + w\frac{\partial}{\partial z} \qquad (2.8)$$

where

- x, y, z are the zonal, meridional and vertical coordinates in the Cartesian frame of reference (in m).

- $\mathbf{u}(u, v, w)$ is the velocity vector with u its zonal, v its meridional and w its vertical component.

- t is the time (in s).

- f is the Coriolis parameter (in s^{-1}).

- g is the gravitational acceleration ($m.s^{-2}$).

- ϕ is the dynamic pressure (in $m^2.s^{-2}$).

- P is the pressure ($N.m^{-2}$).

- ρ is density ($kg.m^{-3}$).

- ρ_0 is the reference seawater density (assumed to be 1024 $kg.m^{-3}$).

- T is the potential temperature (in $°C$).

- S is the salinity (in psu).

- A_v is the vertical mixing parameter.

- F_T is the surface forcing term for short wave solar radiation.

- D_u, D_v are lateral momentum dissipation terms.

- D_T, D_S describe the horizontal and vertical diffusion of temperature and salt.

The latter equations form a set of partial derivative equations, for which we use the following vertical boundary conditions:

- At the surface: z = η

$$A_v \frac{\partial u}{\partial z} = \frac{\tau_S^x}{\rho_0} \tag{2.9}$$

$$A_v \frac{\partial v}{\partial z} = \frac{\tau_S^y}{\rho_0} \tag{2.10}$$

$$A_T \frac{\partial T}{\partial z} = \frac{Q_T}{\rho_0 c_p} \tag{2.11}$$

$$A_S \frac{\partial S}{\partial z} = \frac{(E - P)S}{\rho_0} \tag{2.12}$$

$$w = \frac{\partial \eta}{\partial t} + u \frac{\partial \eta}{\partial x} + v \frac{\partial \eta}{\partial y} \tag{2.13}$$

- At the bottom: z = -H

$$A_v \frac{\partial u}{\partial z} = \frac{\tau_B^x}{\rho_0} \tag{2.14}$$

$$A_v \frac{\partial v}{\partial z} = \frac{\tau_B^y}{\rho_0} \tag{2.15}$$

$$A_T \frac{\partial T}{\partial z} = 0 \tag{2.16}$$

$$A_S \frac{\partial S}{\partial z} = 0 \tag{2.17}$$

$$w = -u \frac{\partial H}{\partial x} - v \frac{\partial H}{\partial y} \tag{2.18}$$

where,

- η is the surface elevation (in m).
- τ_S^x, τ_S^y are surface wind stresses in x and y directions respectively (in $N.m^{-2}$).
- τ_B^x, τ_B^y are bottom friction stresses in x and y directions respectively (in $N.m^{-2}$)
- Q_T is the surface heat flux (in $W.m^{-2}$).
- (E-P) is the equivalent evaporation minus precipitation (in psu).
- C_p is the heat capacity of seawater (in $J.kg^{-1}.°C^{-1}$)

2.1.2 Numerics

Equations presented in the last section were solved using the Regional Ocean Modelling System (Shchepetkin and McWilliams, 2003). ROMS uses a generalised vertical terrain following sigma-coordinate. The vertical coordinate can be configured to enhance resolution at sea surface and/or at sea bottom in order to ensure a good vertical resolution in the surface mixed layer and a topography following coordinate in the interior of the water column. ROMS

has a split-explicit free surface. The default choice for the subgrid-scale vertical mixing is the K-profile planetary (KPP) scheme (Large et al., 1994; Lemarié et al., 2012). Nevertheless, in our study we implemented the General Length Scale Model KKL parametrized as Mellor and Yamada (1982) 2.5 closure, in order to have the same model of turbulent closure over the whole water column. This allowed the development of an active surface and bottom mixed layer. Additionally, the default version of water KPP implemented in the ROMS code lead to unrealistic convection of water masses in the presence of surface heat loss. The prognostic variables of the model are the surface elevation η, the baroclinic and barotropic horizontal velocities $((u, v)$ and $(\bar{u}, \bar{v}))$, temperature and salinity. Note that prognostic equations for the turbulent kinetic energy and the mixing length scale are also solved in order to compute the vertical diffusivity coefficient. Horizontally, ROMS uses curvilinear orthogonal horizontal coordinate, a horizontal staggered "C" grid (Arakawa and Lamb, 1977).

Historically, terrain-following coordinates emerge from the need to model turbulent processes in the surface and bottom boundary layers and simulate flows along topography (Mellor and Yamada, 1982). The attempts led to the development of the widely used Princeton Ocean Model (POM). Similar models followed with the development of the semi-spectral primitive equation model (SPEM, Haidvogel et al. (1991)), the S-Coordinate Rutgers Model(SCRUM,Song and Haidvogel (1994)) and the Regional Ocean Model Systems (ROMS). Earlier versions of the last mentioned models with either vertical spectral schemes or with rigid lid surfaces were replaced by finite three-dimensional differencing and free surface schemes, such as SCRUM. ROMS eventually became very similar to the POM in most aspects (Ezer et al., 2002). ROMS was expanded from SCRUM with a variety of new features, including alternatives for high-order upstream-biased advection, subgridscale parametrization, and high performance computing on SMP-class computer architectures.

2.2 Experiment set up

In order to study the role of topography in the Southern Ocean, we first needed to model a zonal jet with the basic dynamical features of the ACC, *i.e* a zonal current, with a strong barotropic component, associated to a poleward bending of the isopycnes towards the surface, and the generation

of barotropic/baroclinic instabilities sustaining a continuous mesoscale turbulence. We opted for the idealised model set-up of Abernathey et al. (2011). He considered a zonal jet in a east-west periodic channel forced by westward winds and net temperature heat-fluxes chosen to mimic the meridional variation of heat losses and gains observed in nature.

2.2.1 Geometry

We used the same meridional extension as (Abernathey et al., 2011), *i.e* 2000 km. The zonal dimension was extended to 5000 km in order to be able to study topographic obstacle with a typical length scale up to 1000 km. This long zonal extent allowed the ACC to reach equilibrium downstream of the obstacle before anomalies reentered the channel thanks to the east-west periodic conditions. The vertical extent of our domain was increased to 4000 m. All runs presented in this thesis were done with a horizontal resolution of 16 km and 35 sigma-layers, the resolution capable of resolving eddies in this region. The Rossby radius of deformation for the Southern Ocean is approximately 10 - 30 km (Houry et al., 1987). Surface (θ_s) and bottom (θ_b) stretching are chosen to be 5.0 and 0.0 respectively.

2.2.2 Linear equation of state

In the Abernathey et al. (2011) set-up, the nonlinear equation of state (EOS) is substituted by a linear equation of state and the effect of salinity and pressure on density were neglected:

$$\rho = \rho_0(1 - \alpha(T - T_0)), \tag{2.19}$$

where α is the linear thermal expansion coefficient, T_0 the reference temperature, ρ_0 a reference density, and T the prognostic temperature. The choice of this linear equation of state is to simplify the dynamics of our channel. We are not interested in bottom water mass formation and do not need the non linear thermobaric effects to be included. Additionally, we neglect in our study the effect of salinity. We focus on the effect of external forcing and the effect of topography.

2.2.3 Model forcing

The model was forced mechanically by a surface wind stress and thermodynamically by surface heat fluxes. These forcing fields resemble those observed over the Southern Ocean. Heat fluxes are dictated to include a region of cooling in the far south of the domain, heating in the middle of the domain and cooling again in the north. These regions intend to represent the buoyancy loss associated with AABW formation, the buoyancy gain over the ACC, and the buoyancy loss associated with AAIW-SAMW formation north of the ACC front (Figure 2.1 (a)). Figure 2.1(b) depicts the annual mean wind stress as it is observed over the Southern Ocean. Higher winds blow over the ACC region, and decrease further away. Analytical forcing profiles were used to mimic those changes in our study (Figure 2.2). The analytical expressions are as follows:

- For the heat fluxes:

$$Q(y) = -Q_0 \cos((3\pi y)/L_y) \text{ for } y < 5L_y/6, \qquad (2.20)$$
$$Q(y) = 0 \text{ for } y > 5L_y/6 \qquad (2.21)$$

  with $Q_0 = 10$ W.m^{-2}, L_y the meridional length of the channel.

- For the wind stress:

$$\tau_s(y) = \tau_0 sin(\pi y)/L_y, \qquad (2.22)$$

  with τ_0 the wind stress magnitude which we chose to be $\tau_0 = 0.2$ N.m^{-2}.

2.2.4 Bottom Stress

As in Abernathey et al. (2011) we chose a linear bottom drag to accomplish dissipation:

$$\tau_\mathbf{b} = \rho_0 r_b \mathbf{u}_b, \qquad (2.23)$$

where r_b is the bottom drag coefficient and $\mathbf{u}_b$ the horizontal component of the bottom velocity.
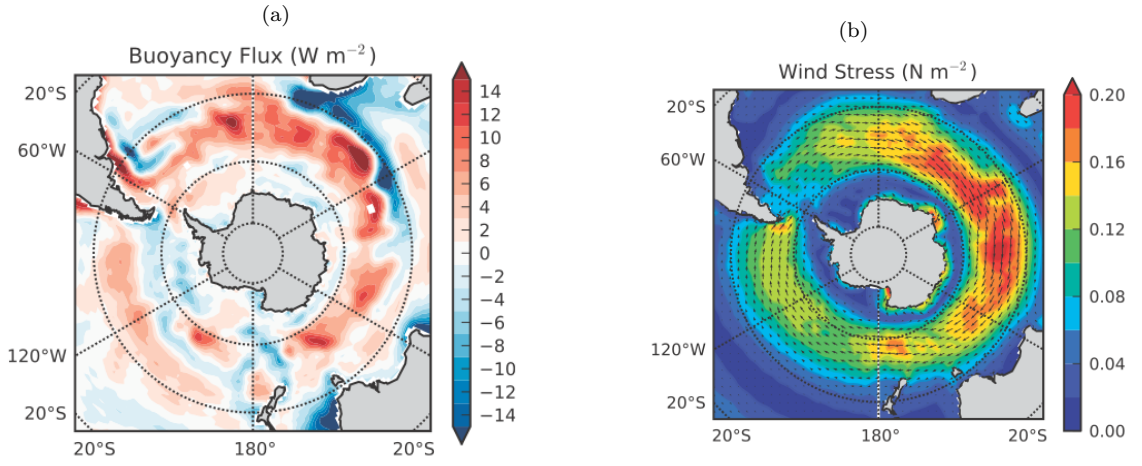
Figure 2.1: Maps of the observed surface forcing in the Southern Ocean, averaged from the Common Ocean Reference Experiment (CORE) data-set over a period of 1949 - 2006. (a) Heat flux(W.m^{-2}) including contributions from long wave and shortwave radiative fluxes, latent and sensible heat fluxes and buoyancy fluxes due to evaporation, precipitation and runoff. (b) wind stress (in N.m^2) with the magnitude indicated by the coloured shading and the direction by the arrows. Adapted from **Abernathey et al. (2011)**.

2.2.5 Boundary conditions

The model includes a sponge layer along the northern boundary of the channel. Inside the sponge layer, the temperature T is relaxed to a prescribed temperature profile:

$$T^*(z) = \Delta T(e^{z/h} - e^{-H/h})/(1 - e^{-H/h}), \qquad (2.24)$$

which depicts an exponential decay from ΔT at the surface to 0 at depth -H with depth scale $h = 100$ m. The relaxation coefficient increases from 0 at the southern edge of the sponge layer (y = L_{sponge}) to 7 day^{-1} at the northern boundary (y = L$_y$). The sponge layer is 100 km. This nudging accounts for the unsolved dynamics of the higher latitudes, especially the slow southward drifting of the North Atlantic Deep Water in the Atlantic Basin.

2.3 Initial Conditions and Spin-up

The model was spin up from rest in 30 years and then integrated another 20 years with outputs every 3 days for the analysis. We initialised our simulations with a stratification similar to the temperature profile used for relaxation at the northern boundary whereby stratification relies on temperature
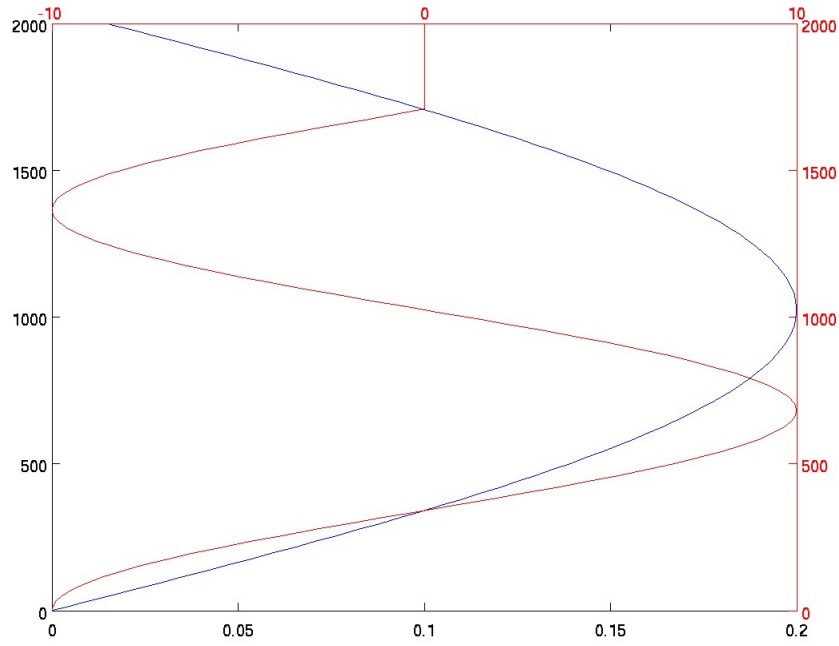
Figure 2.2: Analytical profiles: surface heat flux (red) and surface wind stress (blue). The Y axis is the meridional extent of the domain (km) and the X axis is the amplitude

alone.

$$T^*(z) = \Delta T(e^{z/h} - e^{-H/h})/(1 - e^{-H/h}). \qquad (2.25)$$
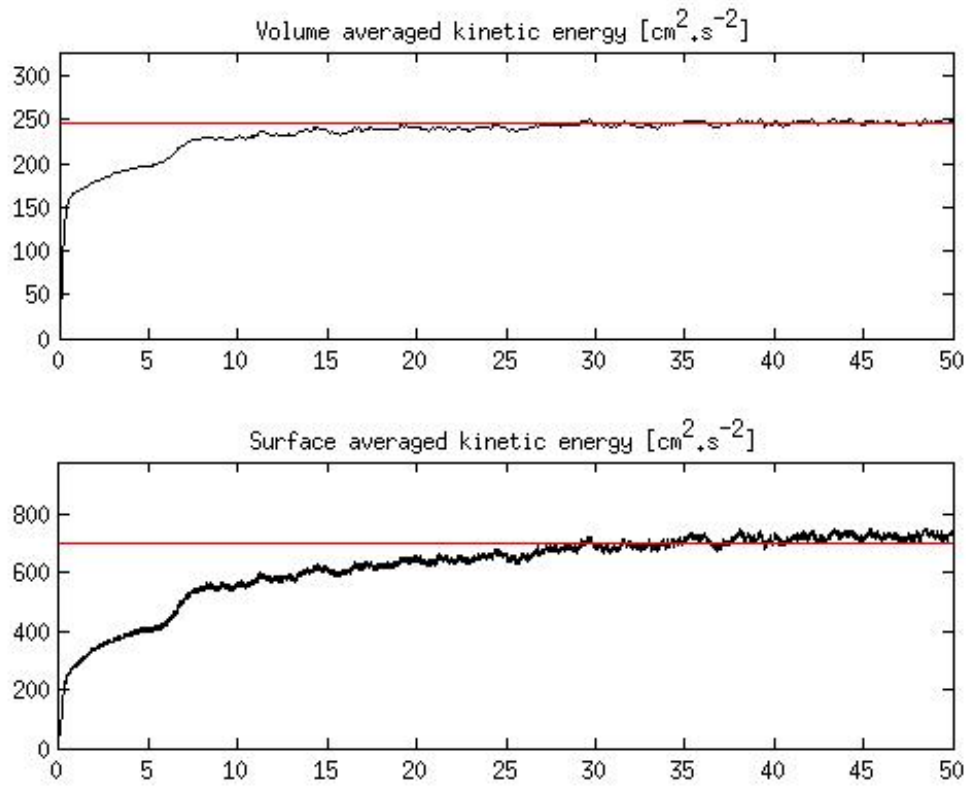
Figure 2.3: Time evolution (in years) of volume integrated kinetic energy for the flat bottom experiment. The time series was made out of 3 days average model outputs.

41

Chapter 3

Results

Introduction

This section is dedicated to the description of the results of our numerical simulations when our zonal jet flows in flat bottom ocean and when it impinges on several topographic obstacles. Four scenarios were considered :

- A flat bed ocean

- A meridional ridge, hereinafter referred as Run_R, characterized by a zonal width of 512 km zonally and heignt of 500 m,

- A square plateau, hereinafter referred as Run_P, with a length scale of 1500 km and a height of 500 m,

- A channel full of randomly scattered seamounts with a typical length scale of 128 km, herinafter referred as Run_S. The method used to initialize our randomly scattered seamounts is presented in the appendix A.

These experiments were performed in order to enquire how the presence of topography may impact the dynamics of the ACC and the characteristics of the mesoscale turbulence. As emphasized in the first chapter, the presence of topography may lead to the deviation of the ACC and to the generation of transient features downstream of the obstacle, like non linear eddies or rossby waves. The numerical simulations were carried out with the same external forcings. They considered different bathymetries that were associated with the same topographic potential vorticity reservoir. In fact, as emphasized in chapter 2, if fluid columns initially located on top of seamounts are moved

towards the open ocean, they will develop a cyclonic circulation. Similarly, if fluid columns initially located besides the seamount are moved over a seamount, they will develop anticyclonic circulation to conserve their potential vorticity. The amount of fluid that can be moved on top of a seamount or away from a seamount by an impinging flow depends on the intensity of the flow, the mean stratification, and the shape of the topography, and obviously the potential vorticity reservoir of the latter:

$$Q_T = \int \int \frac{f}{H - h_T} dx dy, \tag{3.1}$$

with Q_T the potential vorticity reservoir associated to the topography, f the Coriolis parameter, H the depth of the fluid at rest, and h_T the height of the topography. Q_T is the background value of the PV when the fluid is at rest ($\zeta = 0$). In the three simulations, we tested the sensitivity to the shape of the topography keeping the domain integrated topographic potential vorticity reservoir constant. More details can be found in the appendix A.

3.1 Flat bottom equilibrium

The westward wind stress creates a northward Ekman transport that induces the outcrop of the isopycnals in the southern part of our domain. Meanwhile, heat losses in the southern band of the channel deepens the mixed layer depth favouring convection. The combination of the forcing leads to an equatorward progression of the outcrop of the isopycnals. Geostrophic adjustment leads to a zonal current in thermal wind balance with the stratification.

Figure 3.1 shows meridional section of the zonal velocity component and temperature. Fields were averaged over 20 years and zonally. One sees an average zonal current reaching speeds up to 20 cm.s^{-1} at the surface with a strong barotropic component. This current is associated as described previously with the bending of the isotherms.

The barotropic transport computed for the flat bottom experiment was 1000 Sv (Table 3.1), an order of magnitude above the observed value observed in the Southern Ocean. Although not realistic, those values were expected. The absence of topography prevents topographic form drag to balance the input of momentum by the wind stress. And linear bottom friction, on its own, does not succeed in decreasing the zonal barotropic transport to realistic values. The linear bottom coefficient would have to be increased.

A mean eddy kinetic energy (EKE) was also computed for the flat bottom experiment using the last 20 years of our runs with 3 daily outputs. Plots (Figure 3.7) reveal the presence of a strong mesoscale activity linked to the intrinsic instability of the jet itself. The ratio of EKE over MKE (Mean Kinetic Energy) decreases with depth (Table 3.4 and Figure 3.8).

Table 3.1: **Barotropic transport in all the run experiments**. The table shows a decrease in barotropic transport of the current in the presence of topography

Flat bottom	Scattered seamounts	Plateau	Ridge
1000 Sv	555 Sv	450 Sv	270 Sv
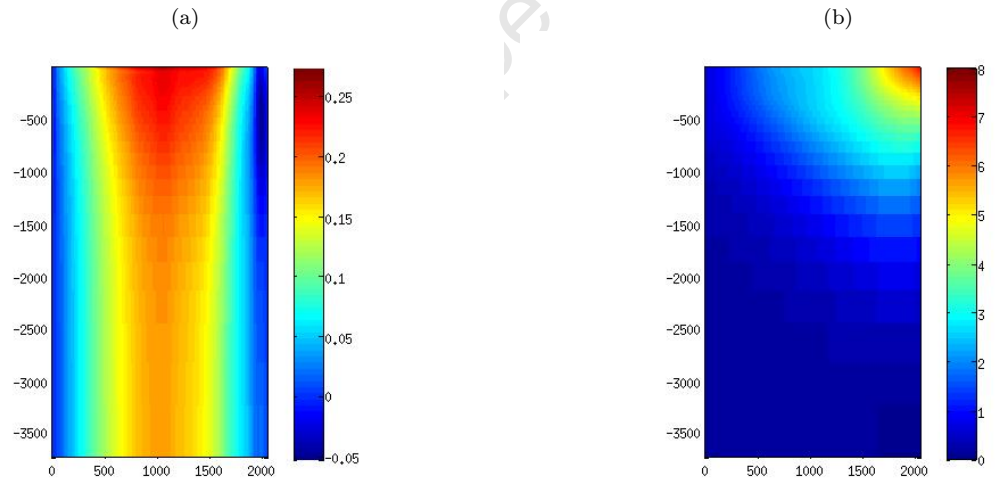
Figure 3.1: Meridional section (Y in km) of zonally averaged time mean: a) velocity (m.s^{-1}) and b) temperature (°C) for the reference no topography experiment.

3.2 Horizontal and vertical structure of the mean flow

Figure 3.2 shows the horizontal mean velocity vectors superimposed with their magnitude at different depths for different bathymetry. Velocities have
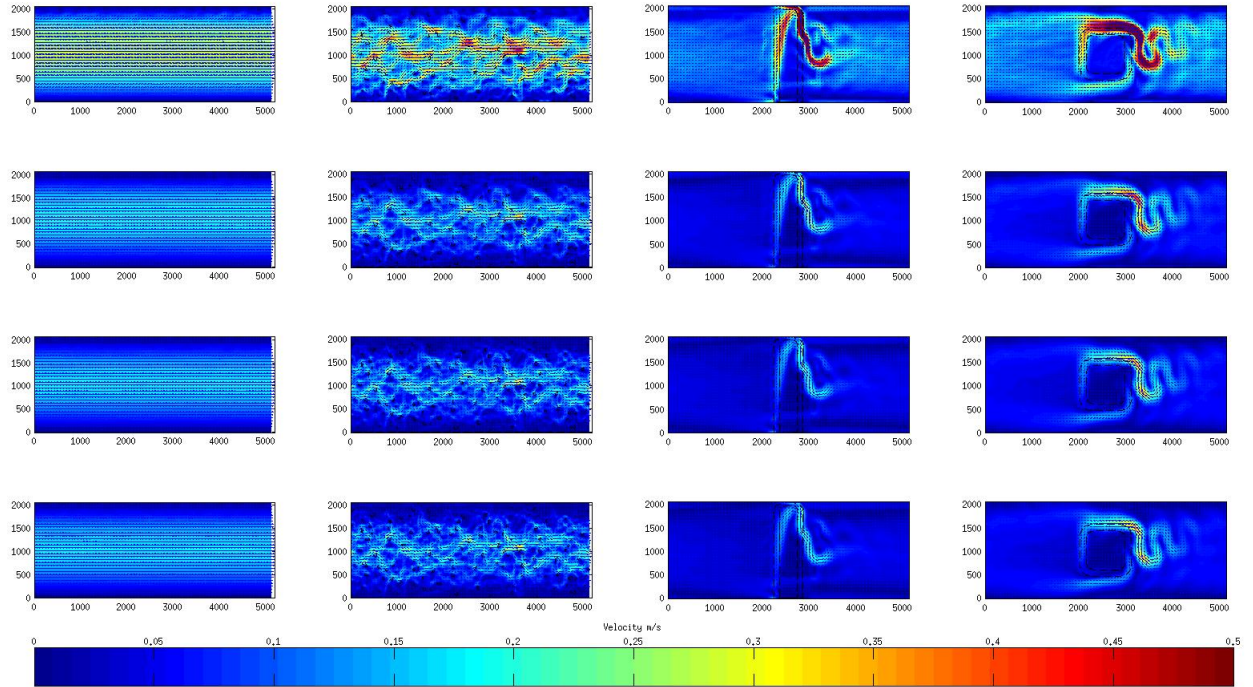
Figure 3.2: 20 years average horizontal velocity vectors superimposed with their magnitude at surface (1st row), 1500 m (2nd row), 2500 m (3rd row), and 3000 m (4th row). Colums refer to runs performed with no topography (1st column), scattered seamounts (2nd column), a ridge (3rd column) and a "plateau" (4th column). X and Y axis are in Km. The colorbar is in m.s^{-1}. A strong zonal jet can be seen at all depths in the no topography and scattered seamounts simulations. For the "ridge" and "plateau" simulations, the zonal jet is mainly deviated equatorward as it impinges on the topography. Then, the path of the jet follows the f/h contours, consistently with the conservation of the barotropic potential vorticity. Before reaching the poleward end of our domain, it bifurcates poleward again before veering towards the east and becoming an estward jet. Downstream of the topographic obstacle, the eastward jet developps large stationary meanders. Note the strong barotropic response of the flow in all our simulations.

45

been averaged over the last 20 years of the simulation. In the abscence of topography, the external forcings were responsible for a strong eastward zonal jet with typical velocities reaching 25 cm.s^{-1} at the surface and decreasing down to 10 cm.s^{-1} at the bottom. This lead to a barotropic zonal transport higher than 1000 Sv, which is well above the realistic 144 Sv observed in the Southern Ocean. In the presence of scattered seamounts, a general zonal mean flow was still clearly visible, although it appeared much more patchy, and looked much more like a muddle of multiple jets flowing around more quiscent local regions. The shape of those jets was closely linked to the position of the seamounts: when impinging on a seamount, the zonal jet would flow around it, leaving a more quiescent region on top of the topography. Within those jets, at all depths, the mean velocities could reach higher values (up to 40 cm.$^{-1}$ at the surface) than in the flat bottom simulation. In the simulations with large isolated topography (ridge and plateau), our ACC deviated equatorward when impinging on the topography. Although, the intensity of the flow decreased with depth, the direction of the flow was consistent over the whole water column, showing evidence of a strong barotropic response. Then, the flow followed the f/h contours, consistently with the conservation of the barotropic potential vorticity. It bifurcated poleward on the eastward edge of the obstacle before veering again towards the east to form an eastward jet. Downstream of the topographic obstacle, the eastward jet developed large stationary meanders, showing evidence of a stationary Rossby wave pattern.

	Y distance	Ro	Fr	L_d	L_d^2/L^2
Upstream	1000 km	0.0013	0.0068	4.7759×10^{04}	0.0348
Downstream	1000 km	0.0016			

Table 3.2: **Computations showing parameter values considered to describe the character of the current flow in Run$_R$, where Ro is the Rossby number, Fr is the Froude number, and L$_d$ is the radius of deformation (H = 500 m and L = 512 km).**

Plots of the mean Sea Surface Height (SSH) are presented in Figure 3.3 for the different simulations. In agreement with geostrophy, good correspondance was found between the observed mean velocities (Figure 3.2) and the shape of the free surface. Higher sea surface heights were found on the left hand side of the flow when going downstream. Rossby numbers were calculated for our flow (Table 3.2 and 3.3). They confirmed that the dynamics
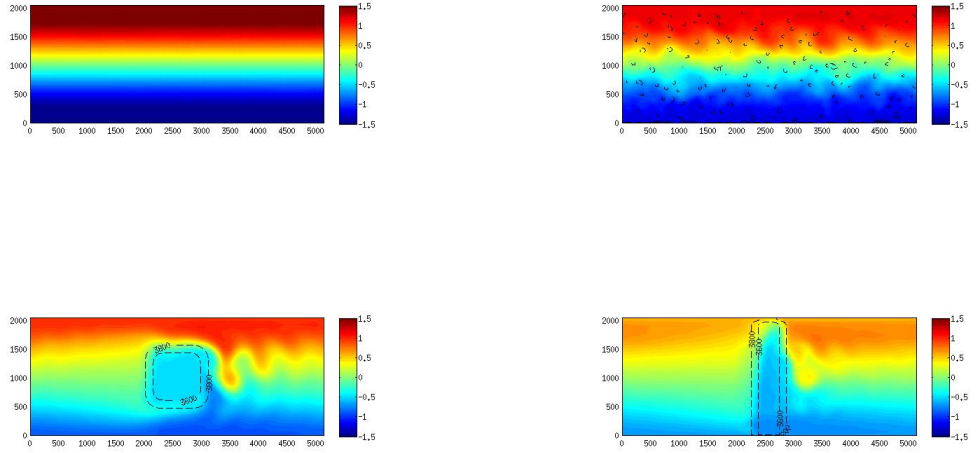
Figure 3.3: Mean Sea Surface Height (SSH) averaged over 20 years for the different bathymetry: flat Bottom (top left), scattered seamounts (top right), plateau (bottom left), ridge (bottom left). SSH in is meters and the X and Y axis are in Km. Sea surface height is consistent with a zonal eastward jet with a strong barotropic component in geostrophic balance. The meridional gradient of SSH is generally directed equatorward. The meanders of the jet that were observed downstream of the isolated topographic features in the velocity vectors (Figure 3.2) have a strong signature in SSH. Note the presence of a trough on top of the plateau and the ridge associated with a cyclonic circulation. In the experiment ran with scattered seamounts, the lines of constant SSH stay rather zonal and seem less affected by the presence topography.

	Y distance	Ro	Fr	L_d	L_d^2/L^2
Upstream	1000 km	4.1561×10^{-04}	0.0082	3.815×10^{04}	0.0026
Downstream	1000 km	8.9158×10^{-04}			

Table 3.3: **Computations showing parameter values considered to describe the character of the current flow in Run_P where Ro is the Rossby number, Fr is the Froude number, and L_d is the radius of deformation (H = 500 m and L = 1500 km).**

of the mean flow was governed by low Rossby number values. Flow associated with low Rossby numbers are close to geostrophic balance. The cyclonic circulation observed around the isolated obstacles (plateau and ridge) was associated to a trough. Similarly, cyclonic/anticyclonic meanders found downstream of the obstacle were associated with troughs/bumps in the SSH. The lines of constant SSH for the flat bottom and the scattered experiment look surprinsingly similar. In the experiment with scaterred seamounts, the isolines of SSH deviated slighly from constant latitudes, and they did not link closely to the complex structure of the multiple jets observed in the plots of the mean velocity (Figure 3.2). Due to lack of time, we did not investigate the causes. Nevertheless, considering that our scaterred seamounts had a typical length scale of 128 km, the deflected flow around them should be roughly in geostrophic balance. Therefore, it is likely that our colorbar did not allow the fine structure of the sea surface height to be represented. Zonal section of the mean temperature averaged over 20 years are presented in Figure 3.4. For the reference experiment without topography, at a given latitude, the isotherms coincided almost perfectly with the geopotential. Vertical deviations could be observed in the presence of bathymetry. For the experiment with the scaterred seamounts, deviations of a few hundreds meters could be observed, with different horizontal length scale. The shorter length scale seemed to correspond to the typical length scale of the seamounts, about a hundred kilometers. Nevertheless, some large scale oscillation also appeared with a typical wave length of a thousand kilometers. The deviations of the isotherms observed in the presence of isolated obstacles were consistent with the shape of the SSH. The cyclonic circulation observed on top of the ridge was associated with an upward bending of the isotherms and a trough in the SSH. Similarly, the anticyclonic and cyclonic meanders observed downstream of the topography were also associated with a downward and upward bending of the isotherms.

Stratification in this study is used as a measure of temperature. Hence, meridional sections of the mean stratification are presented in Figure 3.5 for the experiments with a plateau and a ridge. Sections were performed upstream and downstream of the isolated obstacle. As in the flat bottom experiment (Figure 3.1 (b)), the isotherms tended to outcrop near the poleward end of our domain, given birth to a strong meridional front. Because Rossby numbers associated to the flow were low (Table 3.2 and 3.3), this front was mainly in thermal wind balance and was linked to an eastward jet,
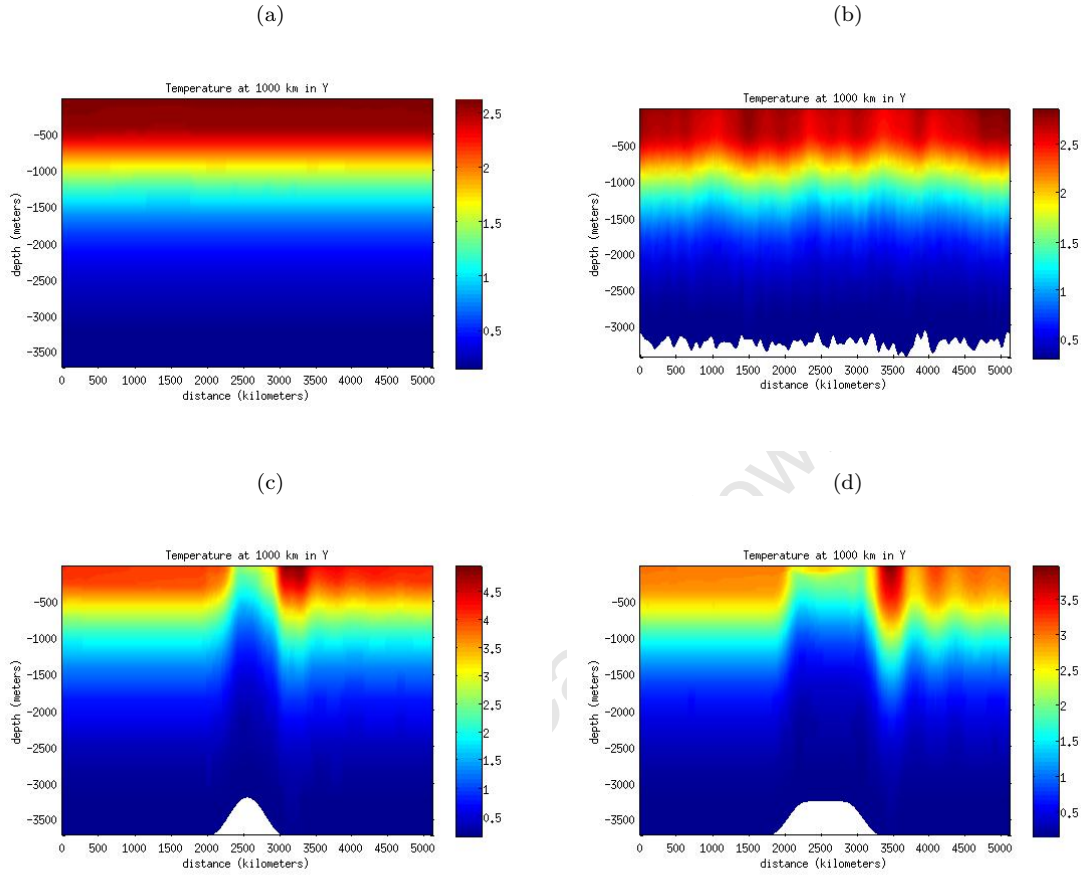
Figure 3.4: Zonal section ($y = 1000$ km) of the mean temperature (°C) averaged over 20 years for our different experiments: (a) no topography, (b) scattered seamounts (c) ridge (d) plateau. Note the uplift of the isopycnals on top of the isolated obstacles (plateau and ridge) is association with the trough observed in the SSH (Figure3.3). The anticyclonic and cyclonic meanders observed downstream of the topography are also associated with an downward and upward bending of the isotherms. The presence of scattered seamounts shows a more complex picture. Although the zonal orientation of the isoterms remains mainly along the geopotential, like in the flat bottom experiment, some deviations occur. Different length scale appear, some short ones (100 km) and some larger ones (1000 km).

our ACC. The meridional position where the isotherms outcroped differed slightly in between the runs. Upstream of the obstacle, a given isotherm outcropped at a higher latitude (closer to the poleward end of our domain) in the experiments with topography than in the flat bottom experiment. Because, upstream of the topographic obstacle, one can consider that the
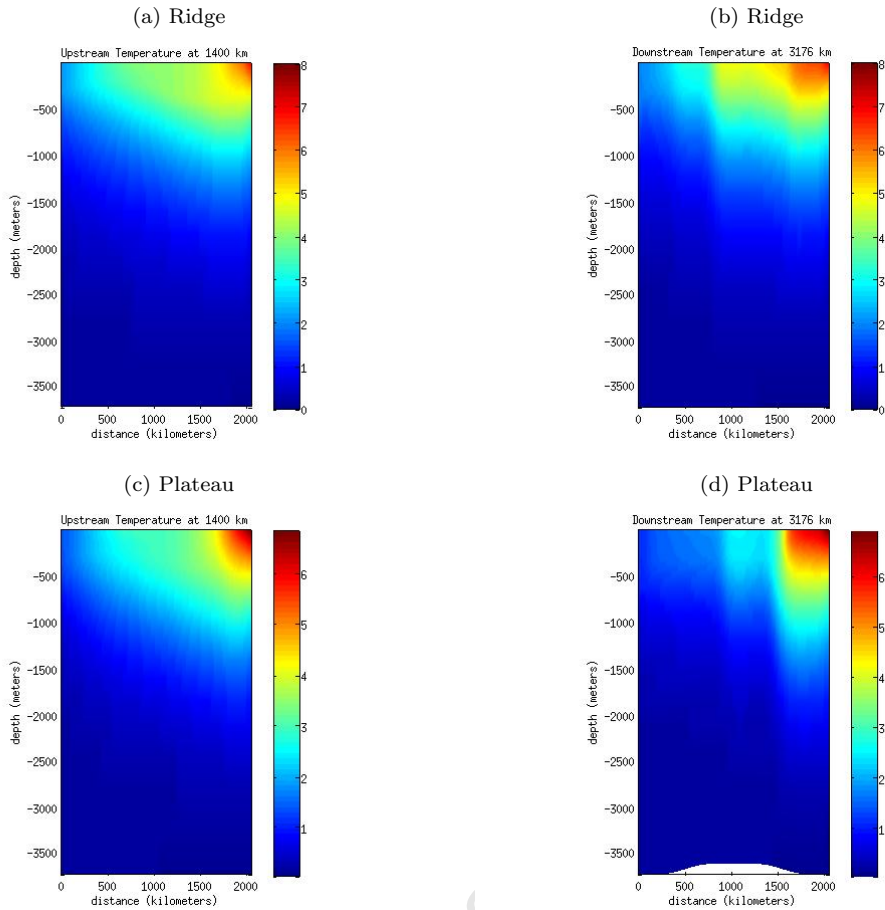
Figure 3.5: Meridional section of the mean temperature (°C) averaged over 20 years for our experiments with the ridge (1ˢᵗ row) and plateau (2ⁿᵈ row). The section is made upstream (a and c) and downstream (b and d) of the isolated obstacle.

transient perturbations (rossby waves and mesoscale eddies) generated by the topography have been dissipated, this observation could be an evidence for stronger horizontal mixing in the runs with topography.

3.3 Transient dynamics

We computed the eddy kinetic energy (EKE) for our different runs out of our 20 years time series of three days outputs. The EKE can be seen as a proxy for the presence of transient dynamical features in our experiments. Horizontal maps of EKE at different depths are shown in Figure 3.6. We also plotted the mean kinetic energy (MKE) (Figure 3.7) and the ratio of the EKE over the MKE (Figure 3.8). Change in the intensity of the EKE do not necessarily indicate the presence of less or more non linear mesoscale eddies. One could imagine two situations with the same quantities of eddies

50
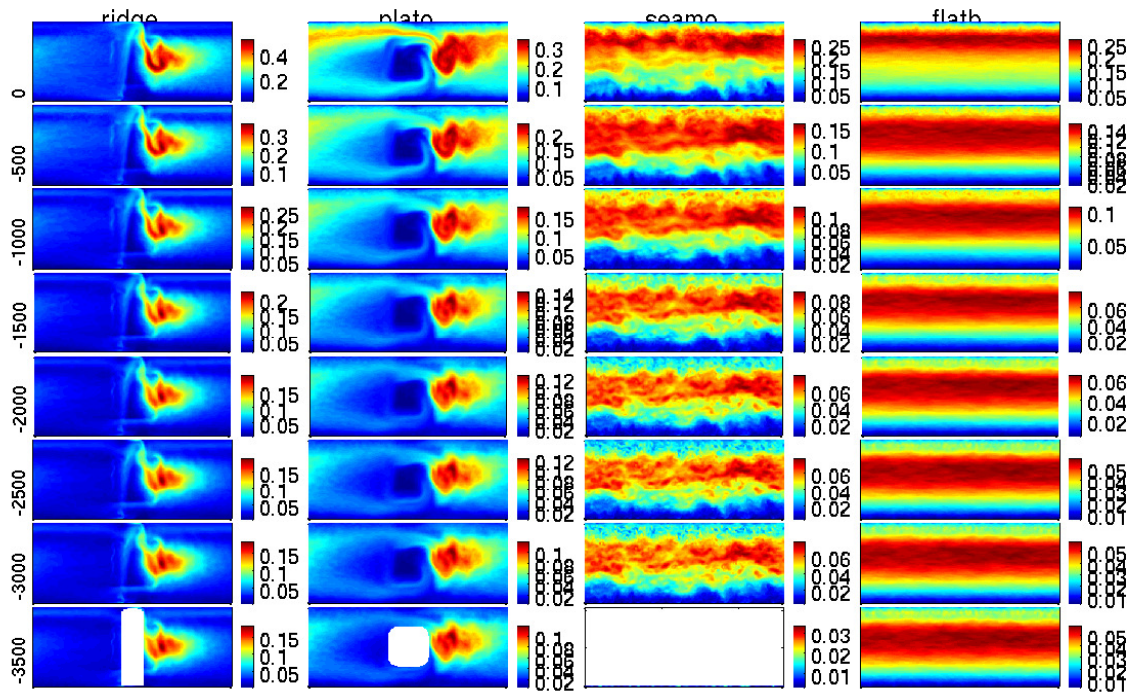
Figure 3.6: Horizontal maps of Eddy Kinetic Energy ($m^2.s^{-2}$) in our different experiments from the surface to -3500 m with a 500 m depths interval (rows). Each column corresponds to given experiment: ridge (1st column), plateau (2nd column), scaterred seamounts (3rd column) and no topography (4th column).

but different EKE if the eddies are for example more intense in one case than the other. This is why, it is sometimes preferable to consider the ratio of the EKE over the MKE. It gives a better idea of how representative the mean flow is at a given instant.
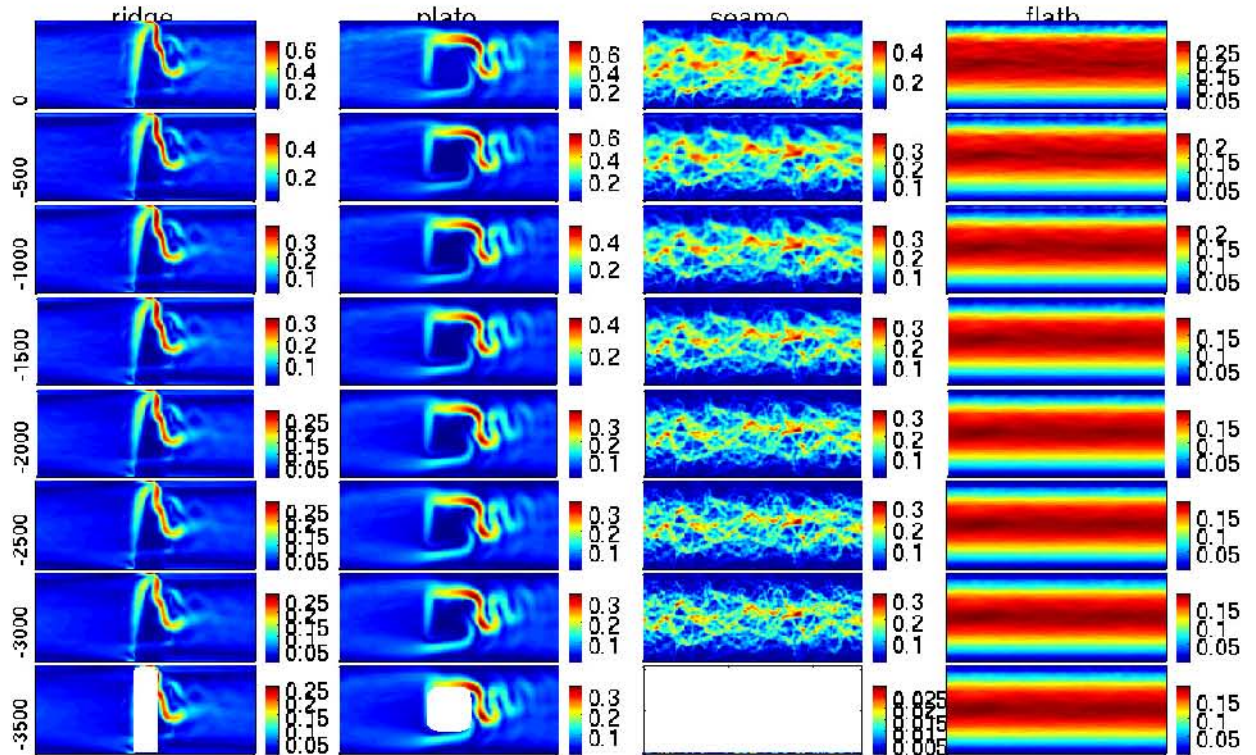
Figure 3.7: Horizontal maps of Mean Kinetic Energy ($m^2.s^{-2}$) in our different experiments from the surface to -3500 m with a 500 m depth interval (rows). Each column corresponds to given experiment: ridge (1st column), plateau (2nd column), scaterred seamounts (3rd column) and no topography (4th column).

As emphasized in our description of the flat bottom experiments (Chapter 2), the meridional density front associated to the ACC was barotropically and baroclinically unstable. These instabilities lead to the generation of non linear mesoscale eddies that were responsible for the observation of high EKE in a latitude band located at the centre of the channel (Figure 3.6). Although, the intensity of the EKE decreased with depth, this region of high EKE was still clearly visible at -3500 m. The presence of topography did not alter this general behavior. A band of high EKE could still be found in that middle latitude band, from the surface to the bottom. In the experiments
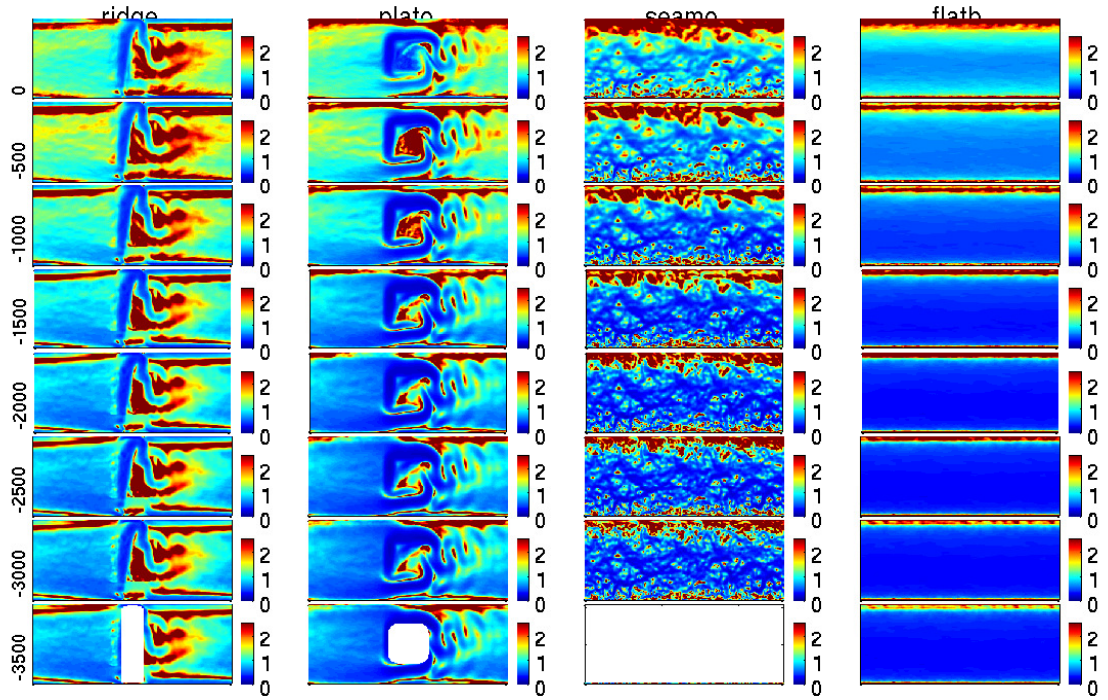
Figure 3.8: Horizontal maps of EKE over MKE in our different experiments from the surface to -3500 m with a 500 m depths interval (rows). Each column corresponds to given experiment: ridge (1st column), plateau (2nd column), scaterred seamounts (3rd column) and no topography (4th column). When EKE/MKE > 1, eddies dominate the mean flow and vice-versa.

with isolated topography, a region of enhanced mean EKE, about twice the background value, could be observed at all depth in the lee of the plateau and the ridge. The high EKE values, found in the specific regions, may come either from small scale instabilities of the jet meanders or the generation of eddies due the advection of fluid particles from above the topography to the open-sea and vice-versa (Herbette et al., 2003; Verron and Le Provost, 1985).

An interesting point can be made by looking at the horizontal maps of EKE over MKE (Figure 3.8) and their horizontally averaged values (Table 3.4). Close to the surface, in all our experiments, this ratio was close to or above one, suggesting that the presence of mesoscale eddies was tremendously important. At depth, the ratio decreased emphasizing the dominance of the mean flow over the transients. In our experiments, the decrease with depth of the EKE over MKE ratio changed differently with depth according to the type of bathymetry. Eddies played a much more important role at

Depth	Ridge	Plateau	Seamounts	Flat Bottom
0m	1.3	1.1	1.0	0.9
-500m	1.3	1.0	0.9	0.7
-1000m	1.0	0.8	0.7	0.5
-1500m	1.0	0.7	0.6	0.4
-2000m	1.0	0.6	0.5	0.3
-3000m	1.0	0.6	0.5	0.3
-3500m				0.3

Table 3.4: Ratio of EKE over MKE for our different runs at several depths. Values correspond to a horizontal average over the whole channel.

depth in the region located in the lee of the plateau and the ridge.

In all our runs, the presence of high EKE region could be noted in the sponge layer located at the equatorward end of our channel. No physical consideration should be given to the variability observed in that layer, whose existence is only to balance the meridional overturning circulation at large time scale, and equilibrate our ACC.

3.4   Vertical velocities and vertical mixing

This work was originally motivated by our wish to understand the possible links between regions of enhanced primary production in the Southern Ocean and the presence of specific topographic features. In the Southern Ocean, the primary production is light and nutrient limited, iron being one of the main limiting factors. One of the iron source comes from the erosion of the topography. Hence, it is mainly present in the deep layers of the ocean, nearby the topographic features. Unfortunately, at these depth, there is no light. Nevertheless, if some physical processes may succeed in uplifting this iron to the euphotic zone, then primary production could be enhanced. These processes could be linked to the presence of intense positive vertical velocities, and/or enhanced vertical mixing nearby seamounts, ridge, plateau. Figures 3.9 and 3.10 represent for different topography the 20 years average meridional section of the vertical velocity and vertical diffusivity coefficient, respectively.

The mean vertical velocities appeared to be very different in our different set-ups. In the reference flat bottom experiment, the mean vertical velocities were generally an order of magnitude smaller than in the experiments with topography ($\simeq 10^{-6}$ m.s^{-1}): upward/downward vertical velocities were
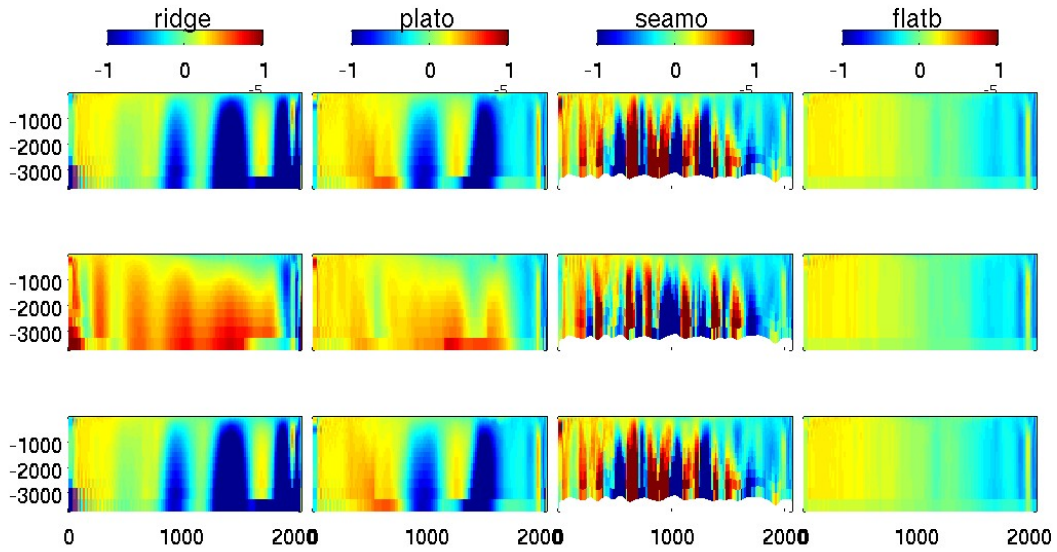
Figure 3.9: Meridional sections of time and meridionally averaged vertical velocities ($\times 10^{-5}$ m.s^{-1}) in our different experiments: ridge (1st column), plateau (2nd column), scattered seamounts (3rd column), flat bottom (4th column). Values have been averaged zonally over the first half of the channel (1st row), the last half of the channel (2nd row), the whole channel length (3rd row)

found on the poleward/equatorward side of the channel. This overwhole picture was consistent with the description of the MOC given by Abernathey et al. (2011). In the scaterred seamounts experiment, this general picture was still valid. Nevertheless, the meridional distribution of vertical velocities appeared to be more patchy, with regions of positive and negative vertical velocities twice the order of magnitude ($\simeq 10^{-4}$ m.s^{-1}) than in the flat bottom experiment. The presence of seamounts could therefore trigger tremendously the uplift of iron to the surface mixed layer in some very localized regions. In the presence of a large scale isolated obstacles like the plateau or the ridge, regions with strong positive/negative vertical velocities could be found upstream/downstream of the isolated obstacle in coherence with the stratification.

Because we only considered the mean vertical velocities, we did not find any link between the regions of enhanced EKE found in the lee of the isolated obstacles and the presence of intense vertical velocities. Plotting the proba-

bility density functions of the vertical velocities using the instantaneous field of our 20 years time series may give a better relation.

The meridional sections of our mean vertical diffusivity coefficient clearly showed the presence of a surface and bottom mixed layer. The surface and bottom mixed layer increased poleward and finally met together at the southern end of our channel in the no topography and scaterred seamounts experiments. This picture was consistent with the presence of surface heat losses at the southern latitudes and the upward branch of the MOC, as described in Abernathey et al. (2011). In the experiments with the plateau and the ridge, the bottom and surface mixed layer surprinsingly did not meet together at the southern end of the channel. One possible explanation may be the decrease of the intensity of the upwelling branch of the MOC in that case. The bottom drag could also be reduced in those experiments in the southern part of the channel due to a shift of the ACC towards the north.

There was no difference in the mean vertical diffusivity coefficient upstream and downstream of the ridge and plateau. The region of enhanced EKE found in the lee of these topographic features did not lead to an increase of vertical mixing. Similarly, the presence of scattered seamounts did not increase vertical mixing. Increasing vertical mixing would actually require the presence of enhanced vertical shear in the horizontal velocity field. The generation of internal waves would certainly contribute to an increase of that shear. According to linear theory (Ferrari and Nikurashin, 2010), a mean flow with bottom velocity U_0 and bottom stratification N can generate radiating internal waves from topographic scales k in the range:

$$\frac{|f|}{U_0} < k < \frac{N}{U_0}. \tag{3.2}$$

For our current setting, ($U_0 = 10$ cm.s^{-1}, $f = 10^{-4}$ s^{-1}, $N = 10^{-3}$ s^{-1}) only topography with typical length scale in between 600 m and 6000 m should generate internal waves. Our horizontal resolution and the typical length scale considered for our topography (> 100 km) obviously prevented the generation of internal waves when our zonal geostrophic jet impinged bathymetric features. In turn, no subsequent vertical shear was created in the flow.
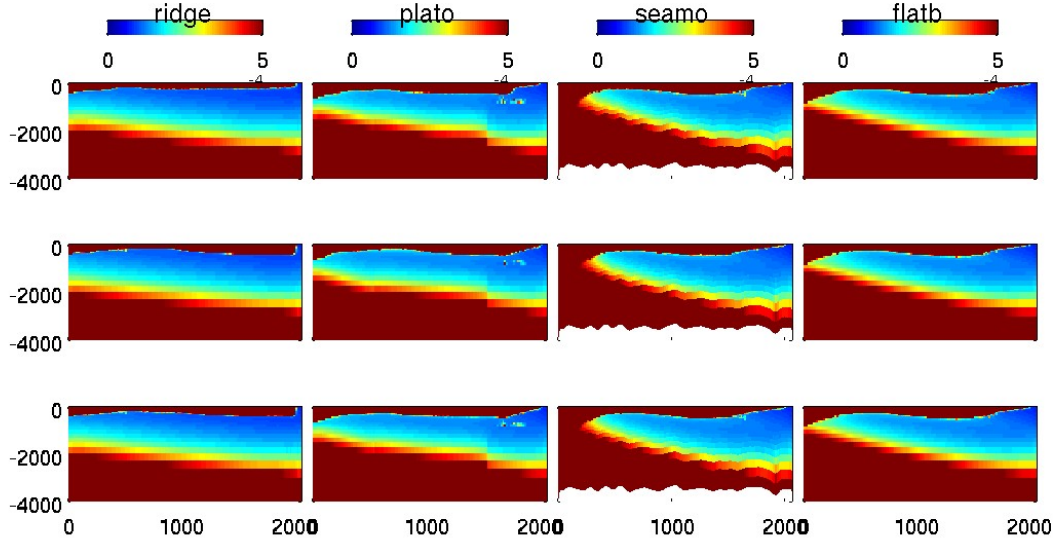
Figure 3.10: Meridional sections of time and meridionally averaged vertical diffusivity coefficient ($\times 10^{-4}$ m^2.s^{-1}) in our different experiments: ridge (1st column), plateau (2nd column), scattered seamounts (3rd column), flat bottom (4th column). Values have been averaged zonally over the eastward half of the channel (1st row), the westward half of the channel (2nd row), the whole channel length (3rd row). As expected, the GLS parametrization that is used for the unresolved vertical turbulent processes computes high vertical mixing coefficients at the surface and at the bottom. These high diffusivity coefficients are then responsible for the generation of surface and bottom mixed layer. At the poleward end of our domain, surface heat losses deepen the mixed layer depth. Within that region, upward vertical velocities also contribute to the upwelling branch of the MOC. In the simulation with no topography or scattered seamounts, the bottom and surface mixed layer match together in the poleward region of our domain.

57

Chapter 4

Oceanic Jet impinging on topography: theory and interpretation of our results

Introduction

The following chapter intends to understand the deviations of mean flow when it impinges on a specific topographic feature according to the existing literature.

4.1 Flow impinging on a topographic obstacle in the case of a homogeneous flow

4.1.1 The Homogeneous equations of motion

In order to better understand the dynamics of a flow impinging on a topographic obstacle, it is first useful to consider the problem in the framework of a homogeneous fluid on the β plane in the absence of friction, external forcing and dissipation. The equations of motion then resume to the well known "shallow-water" equations:

$$\frac{D\mathbf{u}}{Dt} + f\mathbf{k} \times \mathbf{u} = -g\nabla\eta, \tag{4.1}$$

$$\frac{Dh}{Dt} + h\nabla \cdot \mathbf{u} = 0, \tag{4.2}$$

$$\text{with } \frac{D}{Dt} = \frac{\partial}{\partial t} + u\frac{\partial}{\partial x} + v\frac{\partial}{\partial y}. \qquad (4.3)$$

$h = H + \eta - \eta_b$ is the total depth of the water column, η the sea surface height, η_b the topographic height, $f = f_0 + \beta y$ the Coriolis parameter, u and v the zonal and meridional component of the velocity, f_0 the Coriolis parameter at the middle latitude of our domain, and β the linear rate of variation of f with latitude. This set of equations can be non-dimensionalized after defining a typical length scale L, a typical horizontal velocity U and assuming that the flow is close to geostrophic balance in order to get a scaling for the sea surface height. Note that, hereafter, the non-dimensional variables will be defined with primes. Using the following scaling

$$
\begin{align}
(x, y) &= L(x', y'), &(4.4)\\
(u, v) &= U(u', v'), &(4.5)\\
t &= \frac{L}{U}t', &(4.6)\\
\Delta\eta &= \frac{fUL}{g}, &(4.7)\\
\eta_b &= \eta_b^* \eta_b', &(4.8)
\end{align}
$$

with η_b^* the maximum topographic height, the shallow water equations can be written in their non-dimensional form:

$$Ro\left[\frac{\partial \mathbf{u}'}{\partial t'} + (\mathbf{u}' \cdot \nabla)\mathbf{u}'\right] + (1 + \frac{\beta L}{f_0}y')\mathbf{k}' \times \mathbf{u}' = -\nabla\eta', \qquad (4.9)$$

$$Ro\left(\frac{L}{L_d}\right)^2 \frac{D\eta'}{Dt'} + \left[1 + Ro\left(\frac{L}{L_d}\right)^2 \eta' + \frac{\eta_b^*}{H}\eta_b'\right]\nabla \cdot \mathbf{u}' = 0, \qquad (4.10)$$

where $L_d = \sqrt{gH}/f$ is the barotropic deformation radius and $Ro = U/(fL)$. Barotropic deformation radius is defined as the length scale at which rotational effects becomes as important as buoyancy or gravity wave effects in the evolution of a homogenous flow (Gill, 1982). Four non-dimensional parameters appear in this set of equations, meaning that the dynamics of our flow impinging on a topography is entirely governed by four non-dimensional parameters. The latter can be built by any combination of the ones that appear in this set of equations. Nevertheless, before building those numbers, it appears very useful to derive another equation and non-dimensionalize it using the same scaling as before. The relevant non-dimensional parameters governing our dynamics will then become straightforward.

4.1.2 The Potential Vorticity equation for a homogeneous fluid

Taking the curl of the momentum equation and using the mass conservation equation, one can derive the equation of evolution of the potential vorticity (PV):

$$\frac{D}{Dt}PV = 0, \tag{4.11}$$

$$PV = \frac{\zeta + f}{h}, \tag{4.12}$$

with $\zeta = \partial_x v - \partial_y u$ the relative vorticity. This equation has enormous dynamical implications. It implies that a fluid parcel must conserve its potential vorticity in the absence of external forcing, friction and dissipation. In case of flow/topography interactions on the f-plane (constant f), it implies that a water column that climbs on a topographic obstacle develops anticyclonic vorticity, and vice-versa for a water column that is moved away from a topographic obstacle. Note that this equation, assuming that the fluid is in geostrophic balance, can also be inverted to get the entire flow (Hoskin et al., 1985).

In the case of atmospheric and/or oceanic dynamics, it is sometimes useful to define another relevant quantity, the Potential Vorticity Anomaly (PVA):

$$PVA = H \times \left(PV - \frac{f_0}{H} \right), \tag{4.13}$$

H being a constant reference depth hereinafter taken as the depth of the fluid at rest in the absence of topography. It is easy to show that the PVA has the same conservation properties as the PV:

$$\frac{D}{Dt}(PVA) = \frac{D}{Dt}(HPV) - \frac{D}{Dt}f_0 = H\frac{D}{Dt}(PV) = 0.$$

The PVA has the same advantages as PV. It additionally gives a better idea of the sense of circulation of the flow when the fluid is close to geostrophy (small Rossby numbers). In fact, in the ocean, PV at large and meso-scale is dominated by the background PV, f_0/H. Hence, it is not necessarily easy to guess the sign of the circulation (the relative vorticity) just by knowing the value of the PV. Therefore, we prefer to subtract this background value out and multiply the whole expression by a constant depth to define a quantity with the same dimension as f_0. Let's now define Q as the PVA of a given

fluid parcel:

$$Q = H \left(\frac{\zeta + f_0 + \beta y}{H + \eta - \eta_b} - \frac{f_0}{H} \right). \tag{4.14}$$

In the case of small sea surface height deviation ($\eta << H$) and small topography ($\eta_b << H$), the expression of Q writes as follows:

$$Q \simeq (\zeta + f_0 + \beta y) \times \left(1 - \frac{\eta}{H} + \frac{\eta_b}{H} \right) - f_0. \tag{4.15}$$

Assuming the values of ζ, η, η_b, and βy are small, the latter expression can be linearized, which yields:

$$Q = \zeta + \beta y - \frac{f_0}{H}\eta + \frac{f_0}{H}\eta_b. \tag{4.16}$$

We may wonder the meaning of "small". In the ocean, down to the limit of mesoscale processes ($L \simeq 10\ km$), "small" can be interpreted as Rossby numbers smaller than one ($U/(f_0 L) < 1$), $\eta/H < 1$, $\eta_b/H < 1$ and a domain extension that is not too big in order that the β plane approximation remains valid ($\beta L/f_0 < 1$). Equation 4.16 can be non-dimensionalized using the same scaling as for the primitive equations. The non-dimensional form of the PVA evolution becomes:

$$(\partial_{t'} + u'\partial_{x'} + v'\partial_{y'}) \left(\zeta' + \frac{\beta L^2}{U} y' - \frac{f_0^2 L^2}{gH}\eta' + \frac{1}{Ro}\frac{\eta_b^*}{H}\eta_b' \right) = 0 \tag{4.17}$$

This equation can also be written as:

$$(\partial_{t'} + u'\partial_{x'} + v'\partial_{y'}) \left(\zeta' + \frac{\beta L^2}{U} y' - \frac{Fr^2}{Ro^2}\eta' + \frac{1}{Ro}\frac{\eta_b^*}{H}\eta_b' \right) = 0, \tag{4.18}$$

which may also be written as:

$$(\partial_{t'} + u'\partial_{x'} + v'\partial_{y'}) \left(\zeta' + \frac{\beta L^2}{U} y' - \frac{L^2}{L_d^2}\eta' + \frac{\beta_T L^2}{U}\eta_b' \right) = 0. \tag{4.19}$$

with $\beta_T = f_0 \eta_b^*/(HL)$. We immediately see that the flow will be governed by four non-dimensional parameters:

- the Rossby number, defined as the ratio of non linear terms over the coriolis term. A small Rossby number (large coriolis term and small non - linear terms), implies that the flow is geostrophic.

$$Ro = \frac{U}{f_0 L},$$

61

- the Froude number is defined as the ratio of the velocity of the flow over the speed of the surface gravity waves. It is a measure of the importance of stratification. A small Froude number (strong stratification and small velocity), implies that stratification effects are important.

$$Fr = \frac{U}{gH},$$

- a non-dimensional number related to the importance of the change of PV with latitude (the planetary β-effect) over the nonlinear terms

$$\widetilde{\beta} = \frac{U}{\beta L^2},$$

- a non-dimensional number related to the importance of the change of PV due to the topography (the topographic β-effect) over the nonlinear terms

$$\frac{U}{\beta_T L^2}$$

.

These four non-dimensional parameters can be combined together to generate other parameters more commonly used in geophysical fluid dynamics, like the L/L_d. $(L/L_d)^2$ is the inverse of the Burger number, given as the ratio of Froude number over Rossby number. A large Burger number (large Froude number and small Rossby number), implies that stratification restricts vertical motion and is the dominant process. In the case of Burger number equal to 1, it implies that vertical motions are controlled by both stratification and rotation.

4.1.3 Application to our results

Our numerical simulations show that our zonal jet representing the ACC was deviated equatorward when it impinged on a large scale plateau, or a long meridional ridge. We may wonder if we could have guessed this result from the theory. Considering large scale topography and a barotropic flow, we may assume that:

$$\beta L^2/U \simeq \beta_T L^2/U > 1$$

$$\beta L^2/U \simeq \beta_T L^2/U > L^2/L_d^2$$

In that case, the balance in 4.19 is mainly in between the terms relating to changes in the planetary and topographic PV.

$$(\partial_{t'} + u'\partial_{x'} + v'\partial_{y'}) \left(\frac{\beta L^2}{U} y' + \frac{\beta_T L^2}{U} \eta_b' \right) = 0, \qquad (4.20)$$

or in its dimensional form:

$$(\partial_{t'} + u'\partial_{x'} + v'\partial_{y'}) \left(\beta y + \frac{\eta_b}{H} \right) = 0. \qquad (4.21)$$

The latter equation just implies that the flow must follow the f/h contours. Note that this balance is often referred in the literature as the "Planetary Geostrophy equilibrium" (see for example Vallis (2006)). Upstream of the obstacle, as the zonal jet impinges on the ridge or the plateau, the thickness of the water column decreases. Therefore, in order to conserve its PV, the absolute value of f must also decrease. Hence the fluid moves equatorward. Downstream of the topographic obstacle, far enough from the obstacle, the jet may be assumed to have come back to its zonally eastward form and to be in balance with the external forcing. The fluid that moves off the topography before joining this eastward jet must also follow the f/h contour. When moving away from the topography, h increases. Therefore, in order to conserve its PV, the absolute value f must also increase. Hence the fluid has to flow poleward. This fits to our observation, *i.e*, a equatorward flow on the west side-edge of the obstacle, and a poleward flow on the east side-edge. Obviously, this implies a cyclonic circulation to connect the two, which agrees with our results. In the ridge case, as the flow is deviated equatorward, it slowly "climbs" on top of the ridge, and then develops a cyclonic circulation ($\zeta < 0$) before flowing poleward. This cyclonic circulation has a smaller length scale, typically the zonal dimension of the ridge. This zonal length scale may be small enough so that the vorticity term in Equation 4.21 may not be negligible. In terms of PV conservation, the development of cyclonic vorticity while h is decreasing implies that the decrease of $|f|$ must be quicker, which coincides with an equatorward acceleration of the flow on the western side of the ridge. Similarly, a poleward acceleration of the flow must occur on the eastern side of the ridge where the flow in the region is associated with cyclonic vorticity.

4.2 Influence of stratification

The previous section helped us to interpret our results using PV conservation theory in the framework of a homogeneous flow. However, the Southern Ocean is stratified, and our numerical simulations also considered a stratified flow. We may wonder why the homogeneous flow theory allowed us to interpret our results. In the following, we therefore consider the equations of motion and PV conservation theory in a stratified environment.

4.2.1 The primitive equations

In the absence of diabatic forcing, friction or dissipation, the equations of motions for a rotating, Boussinesq, hydrostatic fluid (the so called primitive equations) write as follows:

$$\frac{D\mathbf{u}}{Dt} + f\mathbf{k} \times \mathbf{u} = -\frac{1}{\rho_0}\nabla P, \tag{4.22}$$

$$\frac{\partial P}{\partial z} = -\rho g, \tag{4.23}$$

$$\frac{\partial u}{\partial x} + \frac{\partial v}{\partial y} + \frac{\partial w}{\partial z} = 0, \tag{4.24}$$

$$\frac{D\rho}{Dt} = 0, \tag{4.25}$$

$$\frac{D}{Dt} = \frac{\partial}{\partial t} + u\frac{\partial}{\partial x} + v\frac{\partial}{\partial y} + w\frac{\partial}{\partial z} \tag{4.26}$$

with P the pressure, g the gravity, w the vertical velocity, and other variables having the same definition as in the set of equations described for the homogeneous flow. The main difference from the homogeneous case comes from the thermodynamic equation $D_t\rho = 0$. For a homogeneous flow, the density of the fluid can not vary, neither in space nor in time. Hence, this equation had no impact. For a stratified fluid, it must be considered. In many texts dealing with ocean dynamics (see for example Vallis (2006)), authors use the fact that density variations found in the ocean are small to decompose the density as follows:

$$\rho(x, y, z, t) = \rho_0 + \rho_s(z) + \widetilde{\rho}(x, y, z, t), \tag{4.27}$$

where ρ_0 is a constant density (taken as the surface density), $\rho_s(z)$ the density variation from ρ_0 if the ocean was at rest, and $\widetilde{\rho}(x, y, z, t)$ some variations of density due to the motions of the Ocean. In the Ocean, this decomposition

is very relevant considering that $\rho_S \ll \rho_0$ and $\widetilde{\rho} \ll \rho_S$. Using the following definition for the Brunt-Väisälä frequency,

$$N^2 = -\frac{g}{\rho_0}\frac{\partial \rho_S(z)}{\partial z} \tag{4.28}$$

the thermodynamic equation writes as follows:

$$\frac{D\widetilde{\rho}}{Dt} - \frac{w\rho_0}{g}N^2 = 0. \tag{4.29}$$

The previous set of equations may be written in a non-dimensional form following the same procedure as we did for a homogeneous fluid. Additionally we define $w = \dfrac{UH}{L}w'$ using the incompressible continuity equation, $\widetilde{\rho} = \dfrac{\rho_0 f_0 LU}{gH}\rho'(x', y', z')$ using the thermal wind equation, and $\widetilde{P} = \rho_0 f_0 UL\widetilde{P}'$ using geostrophy and the following decomposition $P(x, y, z, t) = P_0(z) + P_S(z) + \widetilde{P}(x, y, z, t)$:

$$Ro\left[\frac{\partial u'}{\partial t'} + (\mathbf{u}' \cdot \nabla)\,u'\right] - (1 + \frac{\beta L}{f_0}y')v' \;=\; -\frac{\partial \widetilde{P}'}{\partial x'}, \tag{4.30}$$

$$\frac{\partial \widetilde{P}'}{\partial z} \;=\; -\widetilde{\rho}g, \tag{4.31}$$

$$\frac{\partial u'}{\partial x'} + \frac{\partial v'}{\partial y'} + \frac{\partial w'}{\partial z'} \;=\; 0, \tag{4.32}$$

$$Ro\frac{D\rho'}{Dt'} - \left(\frac{Ro}{Fr}\right)^2 w' \;=\; 0, \tag{4.33}$$

with:

- Fr the baroclinic Froude Number

$$Fr = \frac{U}{NH},$$

- Ro the Rossby number

$$Ro = \frac{U}{f_0 L}$$

.

65

The non-dimensional form of the thermodynamic equation can also be written as follows:

$$Ro\frac{D\rho'}{Dt'} - \left(\frac{L_d}{L}\right)^2 w' = 0, \qquad (4.34)$$

$$Ro\frac{D\rho'}{Dt'} - B_u w' = 0, \qquad (4.35)$$

with:

- L_d the baroclinic Rossby deformation radius, defined as the length scale at which rotational effects becomes as important as buoyancy or gravity wave effects in the evolution of a stratified flow (Chelton et al., 1998).

$$L_d = \frac{NH}{f_0}$$

- B_u the Burger number

$$B_u = \frac{Ro^2}{Fr^2} = \frac{L_d^2}{L^2}$$

Three important comments should be made:

1. The presence of a topography appears in the vertical boundary condition of the thermodynamic equation. In the absence of friction, the dimensional form of the vertical velocity at the bottom boundary ($z = \eta_b$) is: $w(z = \eta_b) = \mathbf{u_H} \cdot \nabla \eta_b$, with $\mathbf{u_H}$ the horizontal velocity vector. Therefore, at the bottom the thermodynamical boundary condition becomes:

$$\frac{D\rho}{Dt} - N^2 \mathbf{u_H} \cdot \nabla \eta_b = 0. \qquad (4.36)$$

2. Similarly to the non-dimensional shallow-water equations, four non-dimensional parameters appear in these equations. The non dimensional parameters can be manipulated to have the Rossby number $Ro = U/(f_0 L)$, a number related to the planetary PV gradient $\beta L^2/U$, a number related to the topography, and a Froude number $F_r = U/(NH)$, or a Burger number $L_d^2/L^2 = NH/f_0 L$)

3. Qualitatively, we expect the presence of topography may be felt over the whole water column if the fluid is weakly stratified, $i.e$ the Burger number (< 1) is small. In such a case, the barotropic response of the

66

flow will be dominant. If the case of infinite stratification, obviously the surface layers of the water column will not feel the topography.

4.2.2 Stratified PV equation

The expression for the evolution of PV in a stratified environment can be derived manipulating the previous primitive equations. Here, we just used its expression in the case of a fluid of constant stratification ($\partial_z N = 0$). Because vertical velocities are small, tiling terms are also neglected. The complete derivation can be found in the textbook of Vallis (2006)):

$$\frac{D}{Dt'} \left(\zeta' + \frac{\beta L^2}{U} y' + \frac{1}{Bu} \frac{\partial \widetilde{\rho}'}{\partial z'} \right) = 0 \tag{4.37}$$

We find an expression very similar to the one found for a homogeneous flow, the first term being the relative vorticity of the fluid, the second term being associated to the change of the PV gradient with latitude according to planetary β-effect, and the third one being associated to the stretching terms. Note that the presence of topography appears through the boundary condition at $z = \eta_b$ of that equation.

4.2.3 Application to our results

Considering the length scale of our ridge and plateau, we can argue that the balance will mainly be between the stretching term and the β term. The term related to relative vorticity can be neglected ($\beta L^2/U >> 1$). Because the Burger number in our simulations is small, the effect of stratification is weak. The isopycnals are strongly deflected as the flow impinges on the topography. This deviation is responsible for an uplift of the isopycnals. This uplift of the isopycnals is associated with an equatorward deviation of the flow on the western side of the ridge. Similarly, a poleward deviation of the flow occurs on the eastern side of the when the isopycnals bend down.

McCartney (1976) seek for a dynamical explanation for the deviation of the ACC observed in the Southern Ocean when it impinges on the Kerguelen plateau on the Scotia ridge. Considering the same set of equations, they were able to derive an analytical solution of the flow for different kinds of topography assuming that the ACC was mainly barotropic (small $U(z)$ dependence), had no horizontal shear, and was close to geostrophy. Their analytical solu-

tion was based on the inversion of the PV equation. They also found that in case of large scale meridional ridge, the flow would be deviated equatorward upstream of the obstacle and poleward downstream of the obstacle in order to follow the f/h contours.

Summary and Discussion

The main goal of this dissertation was to investigate how the presence of topography may locally impact the dynamics of the ACC and the characteristics of the mesoscale turbulence. In order to mimic the topographic features found in the Southern Ocean, three different bathymetries were considered in addition to a reference experiment with no topography, a meridional ridge, a square plateau and a channel full of randomly scattered seamounts.

Implementation of an idealized numerical model of the ACC

The first part of the work was to design a numerical configuration capable of reproducing an eastward flow in a stratified environment, with characteristics similar to the ACC. We successfully implemented the Abernathey et al. (2011) configuration using the ROMS model. The ACC was forced in a stratified east/west periodic channel by eastward wind stress and realistic heat fluxes. The eastward flow had an intensity of roughly 25 cm.s^{-1} at the surface, and slowly decreased with depth to reach 10 cm.s^{-1} at the bottom. Due to the absence of topography, the barotropic transport in the flat bottom experiment was well above ($\simeq 1000$ Sv) the observed value in the Southern Ocean ($\simeq 130$ Sv). In fact, Hughes and De Cuevas (2001) showed that bottom pressure torque related to topography is a major ingredient in the balance of the mean flow, and acts as the input of zonal momentum to compensate for the external forcing. As observed in the Southern Ocean, even at medium resolution (16 km in the numerical experiments for a typical Rossby deformation radius $L_d = 60$ km), the eastward flow developed a subsequent level of eddy kinetic energy (EKE). The turbulence was linked to the presence of mesoscale eddies generated by barotropic/baroclinic instabilities. We also implemented a new turbulent closure model, the General Length

Scale Model KKL (Warner et al., 2005; Umlauf and Burchard, 2003) in order to have the same model of turbulent closure over the whole water column. This allowed the development of an active surface and bottom mixed layer. This is a necessary ingredient for future experiments at higher resolutions in which small scale instabilities are known to take place in the surface mixed layer.

Impact of topography

Deviation of the mean flow

In the presence of topography, as expected, the barotropic transport was drastically reduced. Nevertheless, it was still above the observed values in the Southern Ocean. In future experiments, this could be dealt with by increasing the linear friction coefficient in order to take into account subtle effects associated to small scale topography. In all the experiments with an isolated topography, the deviation of the mean flow could be explained by PV conservation theory. In the case of a square plateau and a meridional ridge, the eastward flow was deviated equatorward as it approached the obstacle in order to conserve its potential vorticity by flowing along the f/h contours. In fact, for large obstacles, the dominant term in the PV equation is the change of PV with latitude associated to the earth's sphericity and the change of PV associated to the presence of topography. These results were consistent with analytical solutions derived by McCartney (1976) who also considered a zonal flow impinging a meridional ridge. In the experiment with scattered seamounts, the mean flow looked more like a muddle of distorted jets with a dominant eastward component. When impinging on a seamount, the zonal jet would flow around it, leaving a more quiescent region on top of the topography, which is consistent with the results found by Thompson (2010) in a quasi-geostrophic framework.

Enhancement of EKE

Experiments in this study only considered large scale smooth topography. Nevertheless, the presence of smooth large scale topography was sufficient to generate higher level of EKE and higher EKE/MKE ratios in the deep layers of the flow. In the simulations with the isolated obstacles (ridge and plateau), the regions of higher EKE were localized in the lee of the obstacle,

where the eastward mean flow developed large stationary meanders. It would now be interesting to characterize the mesoscale turbulence in those regions and compare it to the intrinsic turbulence of the eastward flow without topography. Why would the meandering flow generate more turbulence than the original eastward flow ? In the presence of scattered seamounts, higher EKE was also found at depth. Although we did not investigate for the causes of that EKE, we expect the presence of seamounts to trigger the generation of vortices in the deep layers of the flow as fluid parcels are being advected on top of and away from the seamounts (Verron and Le Provost, 1985; Herbette et al., 2003).

Limits of the work

As in any idealized work, many limitations can be found in this work. Let's leave aside the limitations associated to the geometry of the domain, the presence of a sponge layer at the north of the domain, and the absence of variability in the forcing. The latter are out of the scope of this work. These choices were guided by computing power limitations, problems related to numerical stability, and/or simplification of the physics.

Future work

In order to study the possible effects of topography on the vertical fluxes of nutrients. Three main factors should be outlined:

- The relevant non dimensional parameters in the PV equation are the Rossby number $U/(f_0L)$, the Burger number NH/f_0L, and a number related planetary geostrophy $\beta^* = \beta L^2/U$. The experiments that were carried out during the thesis all considered small Rossby and Burger numbers ($\ll 0.01$) and $\beta^* \simeq 1$. There is a need to carry out sensitivity tests for dynamical regimes characterized by higher values of Rossby and Burger numbers, by considering smaller scale topography.

- The numerical experiments that we performed had a horizontal resolution of 16 km and 35 layers in the vertical. Recent studies show that the vertical fluxes can be increased by an order of magnitude in high resolution experiments capable of solving the submesocale turbulence

71

(Lévy et al., 2012; Klein and Lapeyre, 2009; Capet et al., 2008). Future work can consider higher horizontal resolution in the numerical experiments.

The ultimate goal of this study is understanding the link between some regions of high primary production observed in the Southern Ocean and the presence of specific topographic features. From the literature (Tagliabue et al., 2012; Thomalla et al., 2011), it is known that the main limiting factors of primary production in the Southern Ocean is light, nutrients and iron. It is stated that erosion of topography is one of the main iron sources in the Southern Ocean. Unfortunately, it is located at depth where there is no light. Hence, any physical processes that succeeds in uplifting this iron to the euphotic zone would trigger primary production. These processes could be linked to the presence of intense positive vertical velocities, and/or enhanced vertical mixing nearby seamounts, ridge, plateau. Elevated EKE and the formation of recirculation features are known to be mechanisms driving mixing in the Southern Ocean (Thompson, 2010). Thompson and Salée (2012) showed that recirculation regions downstream of topographic features increase surface eddy diffusivity. In the runs with isolated topography, elevated mean EKE was observed at all depth downstream of the plateau and the ridge. In the experiment with scattered seamounts, higher EKE was observed everywhere at depth. Additionally, the meridional distribution of vertical velocities appeared to be more patchy, with regions of positive and negative vertical velocities twice the order of magnitude higher ($\simeq 10^{-4}$ m.s^{-1}) than in the flat bottom simulation. The high EKE values found in these specific regions came either from the presence of smaller scale instabilities of the jet meanders or the generation of eddies due the advection of fluid particles from above the topography to the open-sea. The study did not isolated specifically one mechanism from the other nor quantified the vertical fluxes associated to these processes. Therefore, the next step would be to focus on the quantification of the vertical fluxes in experiments with a broader range of bathymetry, and isolate the physical mechanisms that are responsible for the enhancement of those fluxes. A better understanding on the physical mechanisms and the induced vertical fluxes will surely help in identifying how the Southern Ocean may influence the ocean CO_2 uptake.

Appendix A

Initialization of random topography

The method used to initialize a random field of seamounts is described in the following. Our wish was to keep the domain integral of the PV reservoir associated to the topography constant in all our simulations. Therefore, instead of considering a field of seamounts, we actually considered the initialization of a randomly distributed PV reservoir (f_0/h). The method consisted in prescribing the distribution of the topographic PV reservoir f_0/h in the 2D Fourier space (k, l). An Inverse Fourier Transform (IFT) was then performed to get the distribution of topographic PV in the 2D physical space. The method had been used by McWilliams (1984) to initialize a field of randomly distributed vortices. As in McWilliams (1984), the spectrum was chosen to be large band, isotropic, and centered around a given wave number k_t, which gave the typical horizontal length scale of the seamounts $(\lambda_T = 2\pi/k_T)$. The steps of the method can be resumed as follows:

1. We define the 2D spectrum of q_T in the Fourier space:

$$\widehat{S_{q_T}}(K) = \left(\frac{K}{1 + \left(\frac{K}{k_T}\right)^6} \right)^{\frac{1}{2}} \tag{A.1}$$

   with $K = \sqrt{k^2 + l^2}$.

2. The spectrum was then multiplied by a random phase to get the distribution of topographic PV in the Fourier Space:

$$\widehat{q_T}(K) = \widehat{S_{q_T}}(K) \times \exp\left(i\phi_{random}\right), \tag{A.2}$$

where ϕ_{random} is a random phase.

3. Finally, a 2D IFT provided the randomly distributed PV reservoir:

$$q_T(x, y) = IFT\left[\widehat{q_T}\right] \qquad (A.3)$$

4. Defining the average of the fluid to be H, the height of the randomly distributed seamounts is just:

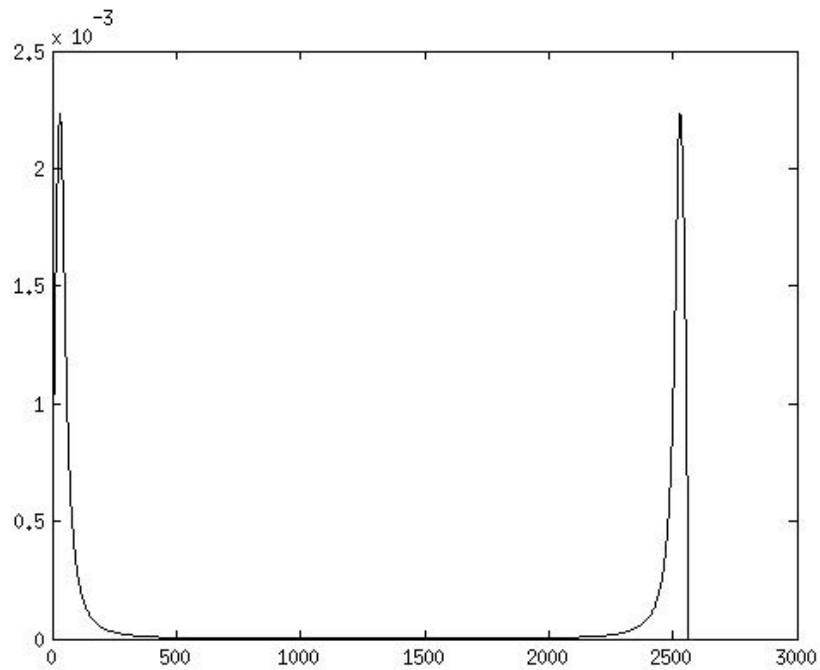$$h_T = \frac{q_T H - f_0}{q_T} \qquad (A.4)$$

Figure A.1: Fourier Space Spectrum

Bibliography

Abernathey, R., Marshall, J., Ferreira, D., 2011. The dependence of southern ocean meridional overturning on wind stress. Journ. Phys. Oceanogr 8, 2261–2278.

Anderson, R., Chasea, Z., Fleishera, M. Q., Sachs, J., 2002. The southern oceans biological pump during the last glacial maximum. Deep Sea Res., Part II 49, 1909–1938.

Arakawa, A., Lamb, V., 1977. Computational design of the basic dynamic process of the ucla general circulation model. Academic. Press.

Capet, X., McWilliams, J. C., Molemaker, M. J., Schepetkin, A. F., 2008. Mesoscale to submesoscale transition in the california current system. part i: Flow structure, eddy flux, and observational tests. jpo.

Chelton, D. B., deSczoeke, R. A., Schlax, M. G., Naggar, K. E., Siwertz, N., 1998. Geographical variability of the first baroclinic rossby radius of deformation. Journ. Phys. Oceanogr.

Cunningham, S. A., Alderson, S. G., King, B. A., 2003. Transport and variability of the antarctic circumpolar current in drake passage. Journ. Geophys. Res 108, 844861.

de Miranda, A. P., B. B., Dewar, W. K., 1999. On the dynamics of the zapiola anticyclone. Journ. Geophys. Res.

Ezer, T., Arango, H., Shchepetkin, F. A., 2002. Developments in terrain-following ocean models: intercomparisons of numerical aspects. Ocean Modelling.

Farneti, R., Delworth, T. L., Rosati, A. J., Griffies, S. M., Zeng, F., 2010. The role of mesoscale eddies in the rectification of the southern ocean response to climate change. Journ. Phys. Oceanogr.

Fauchereau, N., Tagliabue, A., Bopp, L., Monteiro, P. M. S., 2011. The response of phytoplankton biomass to transient mixing events in the southern ocean. Journ. Geophys. Res 38, L17601.

Ferrari, R., Nikurashin, M., 2010. Suppression of eddy diffusivity across jets in the southern ocean. Journ. Phys. Oceanogr.

Gent, P. R., Large, W. G., Bryan, F. O., 2001. What sets the mean transport through drake passage? Journ. Geophys. Res.

Gill, A. E., 1982. Atmosphere - ocean dynamics. Academic. Press.

Gille, S. T., 1997. The southern ocean momentum balance: Evidence for topographic effects from numerical model output and altimeter data. Journ. Phys. Oceanogr 27, 2219–2232.

Gille, S. T., 2003. Float observations of the southern ocean. part i: Estimating mean fields, bottom velocities, and topographic steering. Amer. Meteor. Soc. 33, 1167–1181.

Gnanadesikan, A., Hallberg, R., 2000. On the relationship of the circumpolar current to southern hemisphere winds in coarse-resolution ocean models. Journ. Phys. Oceanogr.

Griesel, A., Gille, S. T., Sprintall, J., McClean, J. L., LaCasce, J. H., Maltrud, M. E., 2010. Isopycnal diffusivities in the antarctic circumpolar current inferred from lagrangian floats in an eddying model. Journ. Geophys. Res.

Haidvogel, D. B., Beckmann, A., Hedström, K. S., 1991. Dynamical simulations of filament formation and evolution in the coastal transition zone. Journ. Geophys. Res.

Herbette, S., Morel, Y., Arhan, M., 2003. Erosion of a surface vortex by a seamount. Journ. Phys. Oceanogr.

Hoskin, B., McIntyre, M., W., R., 1985. On the use and significance of isentropic potential vorticity maps. qjrms.

Houry, S., Dombrowsky, E., De Mey, P., Minster, J.-F., 1987. Brunt-v'ais'al'a frequency and rossby radii in the south atlantic. Amer. Meteor. Soc.

Hovius, N., Meunier, P., Ching-Weei, L., Hongey, C., Yue-Gau, C., Dadson, S., Ming-Jame, H., Lines, M., 2011. Prolonged seismically induced erosion and the mass balance of a large earthquake. Earth Planet. Sci. Lett.

Hughes, C. W., 2005. Nonlinear vorticity balance of the antarctic circumpolar current. Journ. Geophys. Res.

Hughes, C. W., De Cuevas, B. A., 2001. Why western boundary currents in realistic oceans are inviscid: A link between form stress and bottom pressure torques. Amer. Meteor. Soc.

Klein, P., Lapeyre, G., 2009. The oceanic vertical pump induced by mesoscale and submesoscale turbulence. Annu. Rev. Mar. Scie.

Large, W. G., McWilliams, J. C., Doney, S. C., 1994. Oceanic vertical mixing: a review and a model with a nonlocal boundary layer parameterization. rg.

Lavelle, J. W., Mohn, C., 2010. Motions, commotion and biophysical connections at deep ocean seamounts. Oceangr.

Le Quérée, C., Rödenbeck, C., Buitenhuis, E. T., Conway, T. J., Langenfelds, R., Gomez, A., Labuschagne, C., Ramonet, M., Nakazawa, T., Metzl, N., Gillett, N., Heimann, M., 2007. Saturation of the southern ocean co_2 sink due to recent climate. Science.

Lemarié, F., Kurian, J., Shchepetkin, A., Molemaker, M., Colas, F., McWilliams, J., 2012. Are there inescapable issues prohibiting the use of terrain-following coordinates in climate models ? Ocean Modelling.

Levitus, S., Antonov, J., Boyer, T., 2005. Warming of the world ocean. Geophys. Res. Lett.

Lévy, M., 2008. The modulation of biological production by oceanic mesoscale turbulence. Springer. Verlag.

Lévy, M., Resplandy, L., Klein, P., Capet, X., Iovino, D., Ethé, C., 2012. Grid degradation of submesoscale resolving ocean models: Benefits for offline passive tracer transport. Ocean Modelling.

Lu, J., Speer, K., 2010. Topography, jets, and eddy mixing in the southern ocean. Journ. Mar. Res.

Lui, J., Curry, J. A., 2010. Accelerated warming of the southern ocean and its impacts on the hydrological cycle and sea ice. Geophys. Res. Lett.

MacCready, P., Rhines, P. B., 2001. Meridional transport across a zonal channel: topophraphic localization. Journ. Phys. Oceanogr.

Marshall, J., Radko, T., 2003. Residual mean solutions for the antarctic circumpolar current and its associated overturning circulation. Journ. Phys. Oceanogr.

Marshall, J., Speer, K., 2012. Closure of the meridional overturning circulation through southern ocean upwelling. Nature Geosc.

McCartney, M., 1976. The interaction of zonal currents with topography with applications to the. Deep Sea Res.

McWilliams, J. C., 1984. The emergence of isolated coherent vortices in turbulent flow. Journ. Fluid. Mech.

McWilliams, J. C., Holland, W. R., Chow, J. H. S., 1978. A description of numerical antarctic circumpolar currents. Dyn. Atm. Oceans.

Mellor, G., Yamada, T., 1982. Development of a turbulent closure model for geophysical fluid problems. Academic. Press.

Meredith, M. P., C., N. A., Garabato, A. M., Hogg, Farneti, R., 2012. Sensitivity of the overturning circulation in the southern ocean to decadal changes in wind forcing. Journ. Clim.

Munk, W. H., Palmén, E., 1951. Note on the antarctic circumpolar current. Tellus.

Munk, W. H., Palmen, E., 1951. Note on the dynamics of the antarctic circumpolar current. Tellus.

Orsi, A. H., Whitworth III, T. W., Nowlin Jr., W. D., 1995. On the meridional extent and fronts of the antarctic circumpolar. Deep Sea Res.

Peterson, R. G., Whitworth, T., 1989. The subantarctic and polar fronts in relation to deep water masses through the southwestern atlantic. Journ. Geophys. Res.

Rhines, P. B., 2007. 2007. jets and orography: idealized experiments with tip jets and lighthill blocking. Journ. Atmos. Sci.

Rintoul, S. R., Jean Baptiste, S., 2011. Parameterization of eddy induced subduction in the southern ocean surface layer. Ocean Modelling.

Rintoul, S. R., Sparrow, M., Meredith, M. P., Wadley, V., Speer, K., Hofmann, E., Summerhayes, C., Urban, E., Bellerby, R., 2012. The southern ocean observing system: Initial science and implementation strategy. Sci. Comm. on Antarct. Res.

Sallèe, J.-B., Speer, K., Morrow, R., Lumpkin, R., 2008. An estimate of lagrangian eddy statistics and diffusion in the mixed layer of the southern ocean. Journ. Mar. Res.

Sarmiento, J, Toggweiler, J., 1984. A new model for the role of the oceans in determining atmospheric pco$_2$. Nature.

Saunders, P., King, B., 1995. Bottom currents derived from a shipborne adcp on woce cruise in the south atlantic. Journ. Phys. Oceanogr.

Scott, R. B., Wang, F., 2005. Direct evidence of oceanic kinetic energy cascade from satellite altimetry. Journ. Phys. Oceanogr.

Shaffer, H. B., 1993. Phylogenetics of model organisms: The laboratory exolotl, ambystomia mexicanum. Syst. Biols.

Shchepetkin, A. F., McWilliams, J. C., 2003. A method for computing horizontal pressure-gradient force in an oceanic model with a nonaligned vertical coordinate. Journ. Geophys. Res.

Siegenthaler, U., Wenk, T., 1984. Rapid atmospheric co^2 variations and ocean circulation. Nature.

Sloyan, B. M., Rintoul, S. R., 2001. Circulation, renewal, and modification of antarctic mode and intermediate water. Amer. Meteor. Soc.

Song, Y., Haidvogel, D., 1994. A semi-implicit ocean circulation model using a generalized topography-following coordinate system. Journ. Comp. Phys.

Stommel, H., 1957. A survey of ocean current theory. Deep Sea Res.

Straub, D., Killworth, P., M., K., 1993. A simple model of mass-driven abyssal circulation over a general bottom topography. Journ. Phys. Oceanogr.

Sverdrup, H. U., 1947. Wind-driven currents in a baroclinic ocean, with application to the equatorial currents of the eastern pacific. Proc. Natl. Acad. Sci.

Swart, S., Speich, S., Ansorge, I. J., Goni, G. J., Gladyshev, S., Lutjeharms, J. R. E., 2008. Transport and variability of the antarctic circumpolar current south of africa. Journ. Geophys. Res.

Tagliabue, A., Mtshali, T., Bowie, A. R., Swart, S., 2012. A global compilation of over 13,000 dissolved iron measurements: focus on distributions and processes in the southern ocean. BiogeoScie.

Thomalla, S. J., Fauchereau1, N., Swart, S., Monteiro, P. M. S., 2011. Regional scale characteristics of the seasonal cycle of chlorophyll in the southern ocean. BiogeoScie.

Thompson, A. F., 2010. Jet formation and evolution in baroclinic turbulence with simple topography. Journ. Phys. Oceanogr.

Thompson, A. F., Salée, J.-B., 2012. Jets and topography: Jet transitions and the impact on transport in the antarctic circumpolar current. Journ. Phys. Oceanogr.

Treguier, A. M., England, M. H., Rintoul, R. S., Madec, G., LeSommer, J., Molines, J.-M., 2007. Southern ocean overturning across streamlines in an eddying simulation of the antarctic circumpolar current. Ocean. Sci.

Umlauf, L., Burchard, H., 2003. A generic length-scale equation for geophysical turbulence models. Journ. Mar. Res.

Vallis, G. K., 2006. Atmospheric and ocean fluid dynamics: Fundamentals and large-scale circulation. University Press, Cambridge.

Verron, J., Le Provost, C., 1985. A numericalstudyof quasi-geostrophic flow over isolated topography. Journ. Fluid. Mech.

Volkov, D. L., Fu, L.-L., Lee, T., 2010. Mechanisms of the meridional heat transport in the southern ocean. Ocean Dyn.

Warner, J. C., Sherwood, C. R., Arango, H. G., Signell, R. P., 2005. Performance of four turbulence closure models implemented using a generic length scale method. Ocean Modelling.

Wiggins, S., 2005. The dynamical systems approach to lagrangian transport in ocean flows. Annu. Rev. Fluid. Mech.

Witter, D. L., Chelton, D. B., 1998. Eddy-mean flow interaction in zonal oceanic jet flow along zonal ridge topography. Journ. Phys. Oceanogr.

Wolff, J. O., Olbers, D., Mainer Reimer, E., 1991. Wind-driven flow over topography in a zonal β plane channel: A quasigeostrophic model of the antarctic circumpolar current. Journ. Phys. Oceanogr.